

# SOON: Symmetric Orthogonal Operator Network for Global Subseasonal-to-Seasonal Climate Forecasting

Ziyu Zhou<sup>1</sup> Tian Zhou<sup>2</sup> Shiyu Wang James Kwok<sup>3</sup> Yuxuan Liang<sup>1</sup>

## Abstract

Accurate global Subseasonal-to-Seasonal (S2S) climate forecasting is critical for disaster preparedness and resource management, yet it remains challenging due to chaotic atmospheric dynamics. Existing models predominantly treat atmospheric fields as isotropic images, conflating the distinct physical processes of zonal wave propagation and meridional transport, and leading to suboptimal modeling of anisotropic dynamics. In this paper, we propose the Symmetric Orthogonal Operator Network (SOON) for global S2S climate forecasting. It couples: (1) an Anisotropic Embedding strategy that tokenizes the global grid into latitudinal rings, preserving the integrity of zonal periodic structures; and (2) a stack of SOON Blocks that models the alternating interaction of Zonal and Meridional Operators via a symmetric decomposition, structurally mitigating discretization errors inherent in long-term integration. Extensive experiments on the Earth Reanalysis 5 dataset demonstrate that SOON establishes a new state-of-the-art, significantly outperforming existing methods in both forecasting accuracy and computational efficiency.

## 1. Introduction

Subseasonal-to-Seasonal (S2S) climate forecasting, predicting atmospheric conditions from 2 to 6 weeks in advance, is vital for decision-making in energy scheduling, agriculture, and disaster management (Vitart et al., 2017; White et al., 2017; Liu et al., 2025a). However, forecasting on this timescale remains a grand challenge as it occupies the gap between initial-condition-dependent weather prediction and boundary-condition-dependent climate projection,

<sup>1</sup>The Hong Kong University of Science and Technology (Guangzhou), Guangzhou, China <sup>2</sup>DAMO Academy, Alibaba Group, Hangzhou, China <sup>3</sup>The Hong Kong University of Science and Technology, Hong Kong SAR, China. Correspondence to: Yuxuan Liang <yuxliang@outlook.com>.

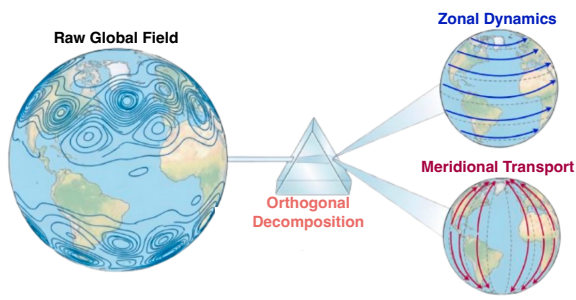


Figure 1. The anisotropic nature of global atmospheric dynamics. Global atmospheric circulation is governed by the coupling of two orthogonal physical processes: Zonal Dynamics, dominated by periodic wave propagation (e.g., planetary Rossby waves), and Meridional Transport, driven by the north-south exchange of heat and momentum (e.g., eddy heat fluxes).

where neither signal alone provides sufficient predictability (Mariotti et al., 2018). Although data-driven models have advanced medium-range (up to 2 weeks) forecasting (Bi et al., 2023; Lam et al., 2023; Price et al., 2025), their direct extensions to S2S protocols typically suffer from rapid error accumulation (Nathaniel et al., 2024; Lyu et al., 2026). This performance gap highlights a fundamental mismatch between the isotropic inductive biases of standard architectures and the anisotropic nature of S2S dynamics.

Recently, data-driven models have achieved strong performance in global S2S climate forecasting (Nguyen et al., 2025). Efforts have adapted to the spherical grid structure via geometry-inspired circular patching strategies (Liu et al., 2025a) or employed equivariant message passing on spherical meshes to handle vector field symmetries (Liu et al., 2025b). Additionally, spectral approaches have been explored to integrate teleconnection modeling with spherical harmonic representations (Lyu et al., 2026) and incorporate Fourier-based embeddings for enhancing wave pattern representations (Li et al., 2025). Collectively, these works have propelled S2S forecasting from empirical statistical models toward end-to-end neural modeling, thereby introducing essential inductive biases for spherical geometry and global dependencies (Chen et al., 2024; Zheng et al., 2025).

A fundamental limitation of existing S2S methods is their reliance on isotropic image modeling, which treats global weather fields as generic 2D images where latitudinal and longitudinal dimensions are processed uniformly. From

a physical perspective, as illustrated in Figure 1, global atmospheric circulation is naturally decomposed into two coupled but distinct mechanisms: zonal periodic wave propagation (Rossby et al., 1939; Hoskins & Karoly, 1981) and meridional transport processes (Peixoto & Oort, 1991; Valllis, 2017). By treating these dimensions uniformly, standard baselines implicitly conflate these distinct physical roles, resulting in insufficient modeling of the true atmospheric dynamics. Crucially, this isotropic assumption also neglects the severe projection distortion inherent in equirectangular grids, causing standard architectures to struggle with the rapid phase variations of planetary waves, particularly in high-latitude regions. Specifically, existing S2S forecasting models are limited by isotropic modeling assumptions, and so standard 2D patching (Li et al., 2025), circular patching (Liu et al., 2025a), and spherical harmonic aggregation (Lyu et al., 2026) fail to explicitly decouple propagation from transport, weakening the representation of complex wave-flow interactions and leading to suboptimal forecasting performance.

Instead of relying on isotropic modeling, we propose the **Symmetric Orthogonal Operator Network (SOON)**, which is designed based on the principles of physical process decoupling and symmetric operator decomposition for effective global S2S climate forecasting. SOON first employs an **Anisotropic Embedding** strategy that tokenizes the grid into latitudinal rings, preserving the integrity of zonal periodic structures while structurally distinguishing them from meridional representations. The core **SOON Blocks** explicitly model the alternating interaction of these processes via a symmetric decomposition, with a **Zonal Operator** capturing global spectral wave dynamics and a **Meridional Operator** modeling local spatial transport. The operators are designed to induce a geometrically orthogonal subspace structure in the representation, thereby aligning the model more naturally with the anisotropic nature of global atmospheric dynamics. Crucially, each SOON block introduces structural symmetry to mitigate the accumulation of discretization errors over the long S2S forecasting horizon. We further adopt a phase-stable normalization scheme tailored for extended forecast windows. Finally, the encoded representation is passed through a lightweight MLP-based **Decoder** that enables forecasts on all atmospheric variables, after which the entire model is trained end-to-end. To our knowledge, SOON is the first S2S forecasting framework that explicitly formulates zonal–meridional decoupling as a symmetric operator-splitting problem in the latent space.

Our main contributions are as follows:

- We identify that prevalent S2S forecasting models fundamentally violate the anisotropic nature of atmospheric dynamics through isotropic modeling, providing a unified perspective on their limitations regarding latitude-

longitude decoupling and operator decomposition.

- We propose SOON for S2S climate forecasting, which integrates Anisotropic Embedding with a symmetric composition of Zonal and Meridional Operators that is theoretically and structurally aligned with long-term atmospheric dynamics at the S2S timescale.
- Extensive experiments on the Earth Reanalysis 5 (ERA5) dataset demonstrate that SOON establishes a new state-of-the-art, outperforming existing methods in both forecasting accuracy and computational efficiency.

## 2. Preliminaries

### 2.1. Problem Definition

We consider global bi-weekly forecasting of  $K$  meteorological variables defined on a latitude–longitude grid. Let  $\Omega = [-90^\circ, 90^\circ] \times [-180^\circ, 180^\circ]$  be the spherical coordinate domain, discretized into  $H$  latitude bands and  $W$  longitude points. We represent the spatial coordinates by  $\mathcal{P} \in \mathbb{R}^{H \times W \times 2}$  with  $\mathcal{P}_{h,w,:} = (\varphi_h, \lambda_w) \in \Omega$ , where  $\varphi_h$  and  $\lambda_w$  denote latitude and longitude, respectively. At time index  $t$  (in days), the global atmospheric state is a tensor  $\mathbf{X}_t \in \mathbb{R}^{K \times H \times W}$ . Following common S2S benchmarking protocols (Mouatadid et al., 2023; Nathaniel et al., 2024), given an initial condition  $(\mathcal{P}, \mathbf{X}_{t_0})$ , our goal is to learn a predictor  $\mathcal{F}_\Theta$  that directly outputs the two verification targets for weeks 3–4 and weeks 5–6:

$$(\hat{\mathbf{Y}}_{15:28}, \hat{\mathbf{Y}}_{29:42}) = \mathcal{F}_\Theta(\mathcal{P}, \mathbf{X}_{t_0}), \quad (1)$$

where  $\hat{\mathbf{Y}}_{15:28} \in \mathbb{R}^{K \times H \times W}$  and  $\hat{\mathbf{Y}}_{29:42} \in \mathbb{R}^{K \times H \times W}$  denote the predicted averages over days 15–28 (weeks 3–4) and days 29–42 (weeks 5–6) relative to the initialization day  $t_0$ , respectively. Our setting focuses on directly estimating these two evaluation-aligned bi-weekly targets from the initialization, in alignment with prior S2S forecasting works (Lyu et al., 2026; Liu et al., 2025a;b; Chen et al., 2024; Mouatadid et al., 2023). A summary of the existing work on weather forecasting and S2S climate forecasting can be found in Appendix A.

### 2.2. Operator Splitting for Non-commutative Dynamics

Atmospheric evolution can be abstracted as a dynamical system defined by the differential equation  $\frac{\partial \mathbf{u}}{\partial t} \equiv \mathcal{F}(\mathbf{u}) = \mathcal{A}(\mathbf{u}) + \mathcal{B}(\mathbf{u})$ , where  $\mathbf{u}(t)$  is the global state vector,  $\mathcal{A}$  and  $\mathcal{B}$  represent different physical processes (e.g., zonal wave dynamics and meridional transport) (Rossby et al., 1939; Hoskins & Karoly, 1981; Peixoto & Oort, 1991).

For easier exposition, we use the linear notation  $\mathcal{F}(\mathbf{u}) = (\mathcal{A} + \mathcal{B})\mathbf{u}$ , in which the exact time- $\tau$  flow can be written as  $\mathbf{u}(t + \tau) = \exp(\tau(\mathcal{A} + \mathcal{B}))\mathbf{u}(t)$ . When the sub-operators do not commute ( $[\mathcal{A}, \mathcal{B}] \neq 0$ ), this flow cannot be factorized into separate evolutions, motivating operator splitting

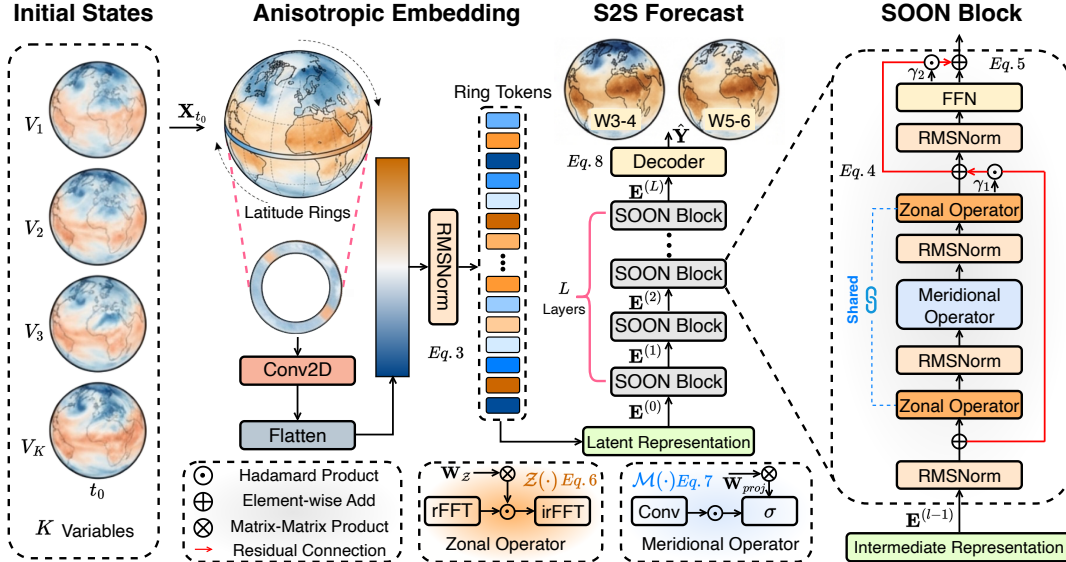


Figure 2. The main architecture of our proposed SOON. The Anisotropic Embedding projects atmospheric initial states into latitudinal ring tokens by compressing the longitudinal dimension into feature channels. These tokens are then evolved through a backbone of several stacked SOON Blocks. Specifically, each block sequentially applies two weight-shared Zonal Operators and a Meridional Operator to explicitly decouple wave propagation and transport dynamics. Finally, a Decoder maps the evolved features to bi-weekly forecast fields.

methods (Trotter, 1959; Strang, 1968; McLachlan & Quispel, 2002). Operator splitting approximates the coupled evolution by alternating simpler sub-evolutions governed by  $\mathcal{A}$  and  $\mathcal{B}$ . Different splitting orders correspond to different discretizations of the same underlying dynamics and lead to distinct error behaviors. In long-horizon forecasting, these error properties matter because local approximation errors can accumulate under repeated composition.

In the following, we introduce two representative operator splitting methods.

**Lie–Trotter splitting (Trotter, 1959).** The first-order decomposition applies the two subflows sequentially, i.e.,  $\mathcal{S}_{\text{Lie}}(\tau) = \exp(\tau\mathcal{B}) \exp(\tau\mathcal{A})$ . By the Baker–Campbell–Hausdorff (BCH) formula (Baker, 1905), its local truncation error is  $\mathcal{O}(\tau^2)$  and is controlled by the commutator  $[\mathcal{A}, \mathcal{B}]$  (Blanes & Casas, 2025).

**Strang splitting (Strang, 1968).** A symmetric second-order decomposition enforces time-reversal symmetry via

$$\mathcal{S}_{\text{Strang}}(\tau) = \exp\left(\frac{\tau}{2}\mathcal{A}\right) \exp(\tau\mathcal{B}) \exp\left(\frac{\tau}{2}\mathcal{A}\right), \quad (2)$$

which cancels the leading second-order BCH terms and yields an  $\mathcal{O}(\tau^3)$  local error (for a sufficiently small time step  $\tau$ ) involving nested commutators (McLachlan & Quispel, 2002). In practice, symmetric decomposition is often preferred when modeling non-commutative systems, as it typically reduces systematic bias and slows down error accumulation compared with sequential decomposition (Hairer et al., 2006; Blanes & Casas, 2025).

### 3. Methodology

Figure 2 illustrates the overall architecture of SOON, which is designed to align neural operations with the anisotropic nature of atmospheric dynamics. The framework is composed of three strategic modules: (i) **Anisotropic Embedding**, which projects the global grid into a sequence of latitudinal ring tokens by compressing longitudinal spatial information into feature channels; (ii) A stack of **Symmetric Operator Blocks** (SOON Blocks), which function as high-order neural solvers via a symmetric Strang splitting scheme, explicitly employing a **Zonal Operator** to capture global spectral wave dynamics and a **Meridional Operator** to model local spatial transport; (iii) A lightweight **Decoder**, which projects the evolved latent representations back to the physical space to generate the final bi-weekly forecasts. The entire architecture is trained end-to-end to minimize the prediction error over the S2S timescale.

#### 3.1. Anisotropic Embedding

Recent data-driven S2S models adopt various patch-based embedding strategies to tokenize global gridded fields, such as circular patching (Liu et al., 2025a), spherical harmonic embedding (Lyu et al., 2026), and Fourier embedding (Li et al., 2025). However, as in conventional approaches (Pathak et al., 2022; Chen et al., 2024), they still treat the atmosphere as an isotropic image, which can disrupt continuous zonal wave structures that are essential for planetary-scale dynamics. This limitation motivates us to design a tokenization strategy that preserves zonal periodicity while decoupling it from the meridional transport processes.

To this end, we introduce Anisotropic Embedding. In

stead of extracting local patches, we project the entire latitudinal ring at each latitude index  $h$  into a single high-dimensional latent token. Formally, given an input state  $\mathbf{X}_{t_0} \in \mathbb{R}^{K \times H \times W}$ , we apply a 2D convolution, operating over the spatial latitude ( $H$ ) and longitude ( $W$ ) dimensions, with a kernel size  $(1, W)$  to compress the longitudinal dimension, followed by flattening and normalization:

$$\mathbf{E}^{(0)} = \text{RMSN}(\text{Flat}(\text{Conv}_{1 \times W}(\mathbf{X}_{t_0}))) \in \mathbb{R}^{H \times C}, \quad (3)$$

where  $\text{Conv}_{1 \times W}$  denotes the convolution operation mapping  $K$  input variables to  $C$  fixed feature channels.  $\text{Flat}(\cdot)$  represents the flattening operation that reshapes the tensor spatial dimension into a sequence of length  $H$ , and  $\text{RMSN}(\cdot)$  denotes Root Mean Square Normalization (RMSNorm) (Zhang & Sennrich, 2019), which stabilizes the latent features without recentering. Consequently, the sequence dimension  $H$  of  $\mathbf{E}^{(0)}$  strictly corresponds to the physical meridional domain, while the feature dimension  $C$  encodes the latent zonal spectral information. Unlike local patching that fragments the grid (Pathak et al., 2022; Li et al., 2025), this global aggregation treats the full longitudinal span as a unified entity, thereby implicitly retaining the intrinsic cyclic topology of atmospheric waves within the latent feature space.

### 3.2. SOON Block

After Anisotropic Embedding, the latent representation  $\mathbf{E}^{(0)}$  is processed through a backbone of  $L$  stacked SOON blocks. Each block functions as a neural operator solver with alternating spectral and spatial operations that advance the atmospheric state by a discrete time step  $\tau$ . We design the internal structure of the block to mimic the symmetric Strang splitting scheme defined in Eq. (2) ( $\mathcal{S}_{\text{Strang}}(\tau) = e^{\frac{\tau}{2}\mathcal{A}}e^{\tau\mathcal{B}}e^{\frac{\tau}{2}\mathcal{A}}$ ). This aims to minimize the discretization error accumulated over long forecast horizons due to non-commutativity of atmospheric operators (McLachlan & Quispel, 2002; Hairer et al., 2006).

Formally, let  $\mathbf{E}^{(l-1)} \in \mathbb{R}^{H \times C}$  be the input to the  $l$ -th block. We define two operators: (i) Zonal Operator  $\mathcal{Z}(\cdot)$ , and (ii) Meridional Operator  $\mathcal{M}(\cdot)$ , that correspond to  $\mathcal{A}$  and  $\mathcal{B}$  in Eq. (2), respectively. Details of these operators will be introduced later in this section. The block updates the representation via a symmetric composition path followed by a Feedforward Network ( $\text{FFN}(\cdot)$ ) with residual connection:

$$\mathbf{E}' = \mathbf{E}^{(l-1)} + \gamma_1 \odot (\mathcal{Z} \circ \mathcal{M} \circ \mathcal{Z})(\text{RMSN}(\mathbf{E}^{(l-1)})), \quad (4)$$

$$\mathbf{E}^{(l)} = \mathbf{E}' + \gamma_2 \odot \text{FFN}(\text{RMSN}(\mathbf{E}')), \quad (5)$$

where  $\circ$  denotes operator composition and  $\odot$  is the element-wise Hadamard product. The parameters  $\gamma_1, \gamma_2 \in \mathbb{R}^C$  correspond to learnable LayerScale (Touvron et al., 2021) vectors that adaptively modulate the signal amplitude in residual branches to facilitate stable training. In Eq. (4),

the Zonal Operator  $\mathcal{Z}$  is applied twice with weight sharing. With this structural symmetry constraint, the SOON block satisfies time-reversal symmetry (Hairer et al., 2006; Blanes & Casas, 2025), which automatically eliminates all even-order error terms (e.g.,  $\mathcal{O}(\tau^2)$ ) in the splitting approximation, thereby directly addressing the error accumulation challenge in long-term forecasting.

The following Theorem provides a theoretical guarantee on error control.

**Theorem 3.1 (Local Truncation Error of SOON Block).**

Let  $\mathcal{L}_{\mathcal{Z}}$  and  $\mathcal{L}_{\mathcal{M}}$  be the infinitesimal generators corresponding to the Zonal and Meridional operators, respectively. Let  $\mathcal{S}_{\text{SOON}}(\tau)$  be the evolution operator of one SOON block approximating the exact dynamics  $e^{\tau(\mathcal{L}_{\mathcal{Z}} + \mathcal{L}_{\mathcal{M}})}$ . By enforcing the symmetric composition  $\mathcal{Z} \circ \mathcal{M} \circ \mathcal{Z}$ , the local truncation error is of third order, i.e.,  $\|\mathcal{S}_{\text{SOON}}(\tau) - e^{\tau(\mathcal{L}_{\mathcal{Z}} + \mathcal{L}_{\mathcal{M}})}\| = \mathcal{O}(\tau^3)$ , which is strictly superior to the  $\mathcal{O}(\tau^2)$  error of standard sequential stacking based on Lie-Trotter splitting.

*Proof.* Based on the symmetric Baker-Campbell-Hausdorff (BCH) (Baker, 1905) formula, the symmetric structure strictly cancels the second-order commutator error terms  $[\mathcal{L}, \mathcal{K}]$  inherent in sequential splitting. See Appendix C.1 for the complete derivation.  $\square$

While Layer Normalization (LayerNorm) (Ba et al., 2016) has been widely adopted in prior S2S forecasting architectures (Liu et al., 2025a;b; Lyu et al., 2026), the following Proposition identifies that its mean-centering operation physically disrupts energy conservation of atmospheric waves.

**Proposition 3.2.** Let  $\mathbf{z} \in \mathbb{R}^C$  be the latent representation of one of the latitudinal ring tokens in  $\mathbf{E}^{(0)}$  from Eq. (3), and let  $\hat{\mathbf{z}} = \mathcal{F}(\mathbf{z})$  be its discrete Fourier spectrum, where  $\mathcal{F}$  denotes the Discrete Fourier Transform (DFT). LayerNorm introduces spectral distortion by eliminating the zero-frequency component (background energy), i.e.,  $|\mathcal{F}(\text{LayerNorm}(\mathbf{z}))_0| \equiv 0$ , where  $\mathcal{F}(\cdot)_0$  represents the 0-th frequency component of the DFT.

In contrast, the following Proposition shows that RMSNorm acts as a uniform spectral scaler. This is critical for S2S forecasting because phase information encodes the spatial positioning and structural topology of planetary waves, which must be preserved to prevent trajectory divergence over long horizons. Accordingly, SOON consistently uses RMSNorm instead of LayerNorm to stabilize training.

**Proposition 3.3 (Spectral Fidelity of RMSNorm).** RMSNorm preserves the phase angles  $\arg(\mathcal{F}(\text{RMSN}(\mathbf{z})))_k = \arg(\hat{\mathbf{z}}_k)$  for all wave numbers  $k$ .

*Proof.* See Appendix C.2 and Appendix C.3 for detailed proof of the propositions above based on the Parseval's theorem (Parseval, 1806) and Fourier Transform.  $\square$

In the following, we detail the implementations of the Zonal and Meridional Operators in each SOON block.

**Zonal Operator  $\mathcal{Z}$ .** It is designed to model global wave propagation (e.g., Rossby waves) along the longitudinal direction. Since our anisotropic embedding compresses longitudinal information into the  $C$  feature channels, zonal dynamics are naturally captured by mixing information across the channel dimension. We implement this via a gating mechanism in the frequency domain:

$$\mathcal{Z}(\mathbf{N}) = \text{iFFT}(\mathbf{W}_{\mathcal{Z}} \odot \text{FFT}(\mathbf{N})), \quad (6)$$

where  $\mathbf{N} \in \mathbb{R}^{H \times C}$  is the normalized input RMSN( $\mathbf{E}^{(l-1)}$ ) in Eq. (4),  $\text{FFT}(\cdot)$  and  $\text{iFFT}(\cdot)$  denote the one-dimensional Fast Fourier Transform and its inverse applied along the feature dimension, respectively, and  $\mathbf{W}_{\mathcal{Z}} \in \mathbb{C}^C$  is a learnable complex weight initialized near identity. By operating in the frequency domain, this operator captures global periodic dependencies with an effective global receptive field (Zhou et al., 2026), preserving phase information critical for wave dynamics while maintaining  $O(C \log C)$  time complexity.

**Meridional Operator  $\mathcal{M}$ .** It targets the latitude dimension  $H$ , where atmospheric dynamics are dominated by local transport (i.e., advection) and thermodynamic mixing rather than global periodicity. We model this via a spatial Gated Linear Unit (GLU) convolution (Dauphin et al., 2017):

$$\mathcal{M}(\mathbf{N}) = (\text{Conv}(\mathbf{N}) \odot \sigma(\text{Conv}_{\text{gate}}(\mathbf{N}))) \mathbf{W}_{\text{proj}}, \quad (7)$$

where  $\sigma(\cdot)$  is the sigmoid function,  $\text{Conv}(\cdot)$  and  $\text{Conv}_{\text{gate}}(\cdot)$  are two distinct 1D convolution layers, both utilizing a fixed kernel size  $k$  sliding over the meridional sequence dimension  $H$ , and  $\mathbf{W}_{\text{proj}}$  is a learnable parameter. The element-wise product  $\odot$  serves as a gating mechanism, allowing the model to dynamically control the information flux, akin to the nonlinear advection terms in fluid dynamic equations (Vallis, 2017), facilitating the learning of local meridional transport patterns.

### 3.3. Decoder

After passing through  $L$  SOON blocks, the latent representation  $\mathbf{E}^{(L)} \in \mathbb{R}^{H \times C}$  contains the evolved atmospheric state in the compressed anisotropic space. The Decoder projects this representation back to the original physical grid to generate the final forecasts. We employ a linear projection layer followed by a tensor reshaping operation to reconstruct the longitudinal dimension  $W$  from the  $C$  feature channels:

$$(\hat{\mathbf{Y}}_{15:28}, \hat{\mathbf{Y}}_{29:42}) = \text{Reshape} \left( \text{Linear}(\mathbf{E}^{(L)}) \right), \quad (8)$$

where the linear layer projects the feature dimension from  $C$  to  $2 \times K \times W$ . Finally, we obtain two tensors,  $\hat{\mathbf{Y}}_{15:28}$  and  $\hat{\mathbf{Y}}_{29:42}$ , each with dimension  $\mathbb{R}^{K \times H \times W}$ , representing the two target bi-weekly mean fields corresponding to weeks 3–4 and weeks 5–6, respectively.

**Training Objective.** The model is trained in an end-to-end manner, minimizing the discrepancy between the predicted bi-weekly means and the ground truth. Based on the target definition in Eq. (1), we define the overall objective  $\mathcal{L}$  as the average squared error over both forecast windows:

$$\mathcal{L} = \frac{1}{2KHW} \left( \left\| \hat{\mathbf{Y}}_{15:28} - \mathbf{Y}_{15:28} \right\|_{\mathcal{L}_2}^2 + \left\| \hat{\mathbf{Y}}_{29:42} - \mathbf{Y}_{29:42} \right\|_{\mathcal{L}_2}^2 \right), \quad (9)$$

where  $\mathbf{Y}_{15:28}$  and  $\mathbf{Y}_{29:42}$  denote the ground truth averaged fields for weeks 3–4 and weeks 5–6, respectively. To account for the spherical geometry of the Earth, the norm  $\|\cdot\|_{\mathcal{L}_2}^2$  represents the latitude-weighted Mean Squared Error, where the error at each latitude  $h$  is weighted by  $w_h = \cos(\varphi_h)$  following (Liu et al., 2025a).

### 3.4. Computational Complexity Analysis

Standard Transformer-based models (Dosovitskiy, 2020; Nguyen et al., 2023) incur a quadratic computational cost of  $\mathcal{O}((HW)^2C)$ , scaling quadratically with the longitudinal resolution ( $W^2$ ). In contrast, SOON achieves a complexity of  $\mathcal{O}(H(C^2 + C \log C + Ck))$  (detailed derivations in Appendix B). Crucially, this complexity is independent of the longitudinal width  $W$  due to our anisotropic embedding. This strictly linear scaling with latitude  $H$  provides a significant efficiency advantage for high-resolution global forecasting compared to isotropic architectures.

## 4. Experiments

### 4.1. Experimental Setup

**Dataset.** Consistent with the established benchmarking protocols (Liu et al., 2025a;b; Lyu et al., 2026), we evaluate SOON on the ERA5 reanalysis dataset (Hersbach et al., 2020), which is widely used as a reference for global atmospheric fields. We regrid the data to a  $1.5^\circ$  resolution, resulting in a  $121 \times 240$  latitude–longitude grid. Following (Liu et al., 2025a;b), we use 63 variables in total. This includes six pressure-level variables (geopotential  $z$ , specific humidity  $q$ , temperature  $t$ , u-wind  $u$ , v-wind  $v$ , and vertical velocity  $w$ ) at ten pressure levels (10, 50, 100, 200, 300, 500, 700, 850, 925, and 1000 hPa), as well as three surface variables (2-meter temperature  $t2m$ , 10-meter u-wind  $u10$ , and 10-meter v-wind  $v10$ ). Following (Liu et al., 2025a;b), we split the dataset chronologically: using 1979 to 2016 for training, 2017 for validation, and 2018 for testing. Detailed descriptions of the dataset can be found in Appendix D.1.

**Baselines.** We benchmark SOON against a wide range of state-of-the-art methods, which can be divided into two categories: (1) **Operational NWP Systems**: including the physics-based models from CMA (Wu et al., 2019), NCEP (Saha et al., 2014), and ECMWF (Molteni et al., 1996). (2) **Data-driven Models**: encompassing foundation models such as PanguWeather (Pangu) (Bi et al., 2023), FourCastNetV2 (FCN2) (Pathak et al., 2022), Cli-maX (Nguyen et al., 2023), and specialized S2S models

**Table 1.** Global S2S climate forecasting results. The best result is in **bold**, and the second-best is underlined. The lower RMSE and higher ACC indicate better performance. We report several key pressure-level variables ( $z500$ ,  $z850$ ,  $t500$ , and  $t850$ ) and single-level variables ( $t2m$ ,  $u10$ , and  $v10$ ). N/A indicates that a baseline does not predict the corresponding variable(s).

Model	RMSE (↓)								ACC (↑)							
	Pressure Level				Single Level				Pressure Level				Single Level			
	$z500(gpm)$	$z850(gpm)$	$t500(K)$	$t850(K)$	$t2m(K)$	$u10(m/s)$	$v10(m/s)$	$z500(gpm)$	$z850(gpm)$	$t500(K)$	$t850(K)$	$t2m(K)$	$u10(m/s)$	$v10(m/s)$		
Weeks 3-4 (Days 15-28)	CMA	69.833	47.056	2.598	2.918	4.221	N/A	N/A	0.968	0.919	0.975	0.974	0.960	N/A	N/A	
	NCEP	68.441	44.787	2.225	2.742	4.028	N/A	N/A	0.969	0.921	0.979	0.977	0.966	N/A	N/A	
	ECMWF	63.674	42.349	2.067	2.391	<b>3.232</b>	N/A	N/A	0.972	0.929	0.982	0.983	0.971	N/A	N/A	
	Pangu	66.224	37.959	2.271	2.569	N/A	2.431	1.984	0.963	0.926	0.966	0.963	N/A	0.812	0.686	
	FCN2	62.755	41.020	2.093	2.390	N/A	2.328	1.896	0.947	0.896	0.966	0.957	N/A	0.830	0.712	
	Transformer	59.748	38.119	2.038	2.531	3.662	2.244	1.793	0.978	0.948	0.983	0.981	<b>0.978</b>	0.840	0.738	
	FNO	68.308	41.014	2.302	2.896	3.912	3.442	2.328	0.965	0.942	0.960	0.942	0.972	0.837	<b>0.742</b>	
	ViT	62.122	39.474	2.249	2.852	4.378	2.379	1.926	0.976	0.945	0.979	0.976	0.969	0.814	0.678	
	ClimaX	59.064	38.420	2.142	3.242	5.342	2.360	2.025	0.978	0.945	0.981	0.971	0.956	0.807	0.649	
	ClimODE	68.767	39.326	2.518	3.147	3.782	2.326	1.793	0.970	0.946	0.972	0.970	0.975	0.827	0.738	
Weeks 5-6 (Days 29-42)	CirT	<b>55.505</b>	<u>34.345</u>	<u>1.931</u>	<u>2.265</u>	5.478	2.253	1.873	0.980	0.955	<u>0.984</u>	0.983	0.958	0.835	0.716	
	EIMP	66.498	41.820	2.312	2.800	4.785	3.683	2.137	<u>0.981</u>	<u>0.956</u>	0.983	<u>0.984</u>	0.974	0.672	0.654	
	TelePiT	59.772	35.199	2.035	2.448	4.002	<u>2.122</u>	<u>1.746</u>	0.977	0.953	0.982	0.980	0.974	<u>0.854</u>	0.741	
	SOON	<b>51.956</b>	<u>33.453</u>	<b>1.824</b>	<b>2.145</b>	<u>3.255</u>	<b>1.994</b>	<b>1.621</b>	<b>0.982</b>	<b>0.958</b>	<b>0.985</b>	<b>0.985</b>	<b>0.982</b>	<u>0.872</u>	<b>0.783</b>	
	CMA	71.400	48.583	2.639	2.933	5.521	N/A	N/A	0.966	0.912	0.974	0.974	0.950	N/A	N/A	
	NCEP	71.332	46.834	2.343	2.833	4.406	N/A	N/A	0.967	0.913	0.977	0.976	0.952	N/A	N/A	
	ECMWF	68.116	45.330	2.177	2.511	4.080	N/A	N/A	0.968	0.916	0.979	0.981	0.970	N/A	N/A	
	Pangu	76.939	47.041	2.829	2.998	N/A	2.679	2.104	0.956	0.911	0.958	0.957	N/A	0.783	0.655	
	FCN2	66.531	43.469	2.250	2.567	N/A	2.479	1.980	0.943	0.889	0.963	0.953	N/A	0.812	0.691	
	Transformer	59.970	38.433	2.065	2.568	<u>3.454</u>	2.279	1.824	0.977	0.947	0.983	0.981	<b>0.980</b>	0.836	0.725	
	FNO	72.021	44.327	2.564	3.334	4.301	2.426	2.084	0.960	0.949	0.971	0.971	0.968	0.840	0.720	
	ViT	63.031	39.825	2.287	2.974	4.469	2.397	1.979	0.976	0.944	0.979	0.970	0.968	0.815	0.641	
	ClimaX	58.712	38.271	2.141	3.300	5.354	2.394	2.031	0.978	0.945	0.982	0.971	0.956	0.800	0.643	
	ClimODE	68.218	39.287	2.554	3.213	4.094	2.336	1.844	0.971	0.946	0.972	0.969	0.971	0.829	0.717	
	CirT	<u>55.214</u>	<u>33.940</u>	<u>1.920</u>	<u>2.265</u>	5.652	2.251	1.826	0.980	0.956	<u>0.984</u>	<u>0.983</u>	0.954	0.835	<u>0.726</u>	
	EIMP	66.856	41.926	2.329	2.858	5.018	2.555	2.155	<u>0.981</u>	<u>0.957</u>	0.983	0.983	0.972	0.792	0.651	
	TelePiT	58.770	35.164	1.953	2.451	4.056	<u>2.120</u>	<u>1.750</u>	0.978	0.953	0.982	0.981	0.975	<u>0.854</u>	0.741	
	SOON	<b>52.268</b>	<u>33.437</u>	<b>1.830</b>	<b>2.156</b>	3.231	<b>1.993</b>	<b>1.606</b>	<b>0.982</b>	<b>0.958</b>	<b>0.985</b>	<b>0.985</b>	<b>0.982</b>	<u>0.873</u>	<b>0.786</b>	

including CirT (Liu et al., 2025a), EIMP (Liu et al., 2025b), TelePiT (Lyu et al., 2026), and ClimODE (Verma et al., 2024). Additionally, we compare against general-purpose backbone models: Transformer (Vaswani et al., 2017), Fourier Neural Operator (FNO) (Li et al., 2020), and Vision Transformer (ViT) (Dosovitskiy, 2020). We adapt these general-purpose models to the S2S forecasting task by modifying their input and output projection heads to accept the global grid tensor while maintaining their original backbone architectures to process the tokenized spatiotemporal sequences. We do not compare with TianQuan-S2S (Li et al., 2025), which uses a different forecasting horizon, and OmniCast (Nguyen et al., 2025), which operates at a different spatial resolution than ours. See details in Appendix D.2.

**Metrics.** Following existing evaluation standards (Rasp et al., 2020; Nathaniel et al., 2024), we employ the Latitude-weighted Root Mean Square Error (RMSE) and Anomaly Correlation Coefficient (ACC) to quantify performance (Nathaniel et al., 2024), defined as:

$$\text{RMSE} = \sqrt{\frac{1}{HW} \sum_{h,w} \alpha(h) (\hat{\mathbf{X}}_{h,w} - \mathbf{X}_{h,w})^2},$$

$$\text{ACC} = \frac{\sum_{h,w} \alpha(h) \hat{\mathbf{X}}_{h,w}' \mathbf{X}_{h,w}'}{\sqrt{\sum_{h,w} \alpha(h) (\hat{\mathbf{X}}_{h,w}')^2} \sqrt{\sum_{h,w} \alpha(h) (\mathbf{X}_{h,w}')^2}}, \quad (10)$$

where  $\alpha(h) = \cos(\phi_h) / (\frac{1}{H} \sum_{h'} \cos(\phi_{h'}))$  represents the latitude weighting factor.  $\mathbf{X}$  and  $\hat{\mathbf{X}}$  denote the ground truth

and prediction for a given bi-weekly verification window. The anomalies are computed as  $\mathbf{X}' = \mathbf{X} - \mathbf{C}$  and  $\hat{\mathbf{X}}' = \hat{\mathbf{X}} - \mathbf{C}$ , where  $\mathbf{C}$  is the observational climatology.

**Implementation Details.** For PanguWeather and FourCastNetV2, we utilize the official pre-trained weights provided by the ECMWF project through API (see Appendix D.2 for details). For the other baselines (except the Operational NWP Systems CMA, NCEP, ECMWF), we train them from scratch using a unified experimental setting to ensure fair comparison (batch size 32, hidden dimension 256, 16 attention heads, and trained for 20 epochs using the AdamW optimizer with an initial learning rate of 0.01). The implementation is based on PyTorch Lightning and training is conducted on 8 NVIDIA H20 80G GPUs. Inference is performed on a single NVIDIA H100 80G GPU. More implementation details are in Appendix D.3.

## 4.2. Overall Performance

Table 1 shows the quantitative comparison against operational NWP systems and state-of-the-art data-driven baselines. As can be seen, SOON consistently achieves the best performance across almost all evaluated metrics, surpassing the leading operational systems, pretrained climate foundation models, general purpose models, as well as recent data-driven climate forecasting models by a substantial margin. Notably, SOON demonstrates exceptional robustness in the extended weeks 5–6 window, maintaining high ACC and low RMSE while other methods suffer from signifi-

Table 2. Ablation study quantifying the contribution of each SOON component. We evaluate variants by removing Anisotropic Embedding (w/o AE), Zonal Operator (w/o ZO), or Meridional Operator (w/o MO), and by replacing RMSNorm (w/o RN) with LayerNorm (w/ LN).

Model	RMSE (↓)										ACC (↑)									
	Pressure Level					Single Level					Pressure Level					Single Level				
	$z500(gpm)$	$z850(gpm)$	$t500(K)$	$t850(K)$	$t2m(K)$	$u10(m/s)$	$v10(m/s)$	$z500(gpm)$	$z850(gpm)$	$t500(K)$	$t850(K)$	$t2m(K)$	$u10(m/s)$	$v10(m/s)$						
Weeks 1-4	<b>SOON</b>	<b>51.956</b>	<b>33.453</b>	<b>1.824</b>	<b>2.145</b>	<b>3.255</b>	<b>1.994</b>	<b>1.621</b>	<b>0.982</b>	<b>0.958</b>	<b>0.985</b>	<b>0.985</b>	<b>0.982</b>	<b>0.872</b>	<b>0.783</b>					
	w/o AE	63.472	41.836	2.618	3.041	4.356	3.604	3.052	0.958	0.921	0.946	0.914	0.952	0.828	0.732					
	w/o ZO	61.207	39.118	2.467	2.742	4.061	3.053	3.441	0.970	0.939	0.953	0.934	0.961	0.818	0.721					
	w/o MO	64.218	42.507	2.334	3.176	4.119	3.284	3.121	0.955	0.926	0.962	0.908	0.958	0.844	0.764					
	w/ unshared ZO	54.124	35.021	1.940	2.217	3.421	2.128	1.822	0.968	0.956	0.977	0.980	0.976	0.860	0.776					
Weeks 5-6	w/o RN, w/ LN	62.948	40.917	2.412	2.957	4.047	3.067	3.302	0.968	0.932	0.959	0.924	0.966	0.856	0.777					
	<b>SOON</b>	<b>52.268</b>	<b>33.437</b>	<b>1.830</b>	<b>2.156</b>	<b>3.231</b>	<b>1.993</b>	<b>1.606</b>	<b>0.982</b>	<b>0.958</b>	<b>0.985</b>	<b>0.985</b>	<b>0.982</b>	<b>0.873</b>	<b>0.786</b>					
	w/o AE	63.761	43.284	2.512	2.913	3.982	3.617	2.621	0.965	0.938	0.954	0.942	0.964	0.834	0.742					
	w/o ZO	61.543	40.643	2.721	2.783	3.889	3.318	2.952	0.974	0.936	0.951	0.953	0.963	0.821	0.728					
	w/o MO	62.872	44.019	2.407	2.792	3.771	3.544	2.386	0.961	0.949	0.960	0.938	0.971	0.846	0.759					
	w/ unshared ZO	55.213	36.221	1.960	2.322	3.501	2.012	1.708	0.970	0.950	0.978	0.980	0.980	0.862	0.766					
	w/o RN, w/ LN	63.318	42.674	2.581	2.979	4.107	3.702	2.561	0.970	0.952	0.967	0.936	0.973	0.857	0.772					

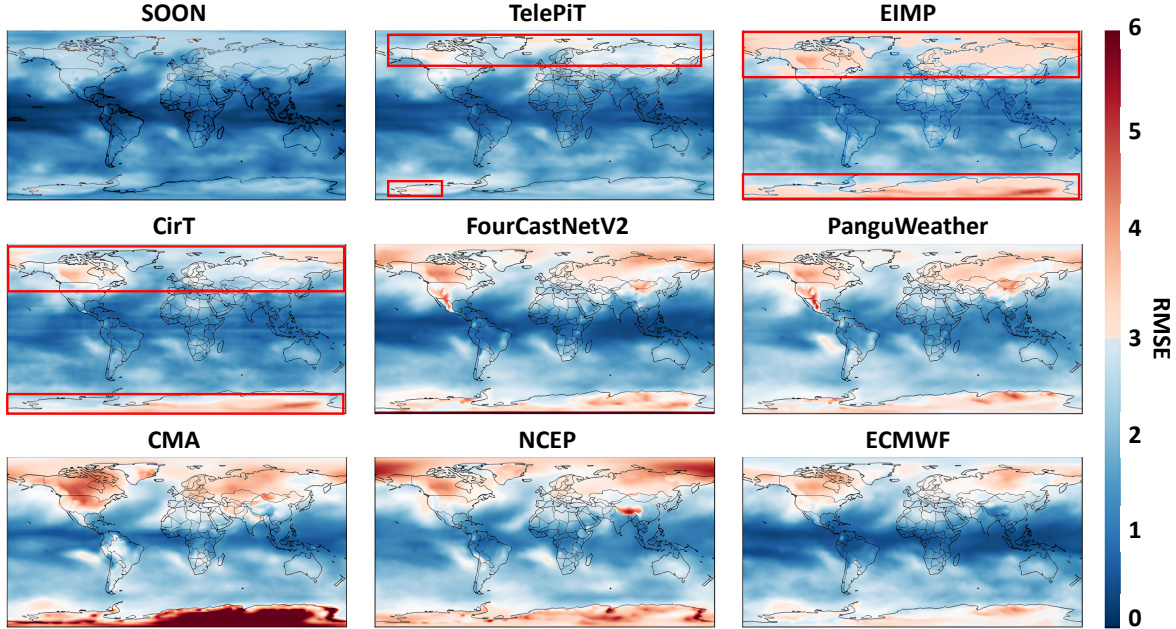


Figure 3. The global RMSE distribution of  $t850$  with lead times weeks 3-4 in the testing set.

cant degradation. This consistent superiority validates that our anisotropic modeling of wave-flow dynamics combined with the symmetric operator splitting scheme can effectively mitigate the accumulation of errors inherent in long-term iterative forecasting. Furthermore, SOON exhibits comprehensive strength across diverse physical regimes, ranking first in both stable upper-air fields and highly chaotic surface variables. We also evaluate SOON with various values of  $L$  (the number of SOON blocks), and the results are presented in Appendix E.1. Additional comparisons on spectral energy distribution are provided in Appendix E.2.

### 4.3. Ablation Study

To validate the effectiveness of our design choices, Table 2 compares SOON with variants with several crucial components removed. The detailed experimental settings are in Appendix D.3. The results show that removing Anisotropic Embedding causes the most severe performance degradation across all variables, confirming that standard isotropic patching disrupts continuous zonal wave structures essen-

tial for S2S dynamics. Similarly, omitting either Zonal Operator or Meridional Operator leads to significant error increases, validating the necessity of explicitly decoupling spectral wave propagation from spatial transport. Additionally, using an unshared-weight Zonal Operator also leads to worse performance, indicating that the symmetric structure of SOON numerically reduces error. Furthermore, the variant using LayerNorm consistently underperforms the RMSNorm baseline, which empirically supports our theoretical analysis that RMSNorm better preserves background energy for long-term integration.

### 4.4. Empirical Analysis

**Global Visualization.** Figure 3 visualizes the spatial distribution of RMSE for  $t850$ . A striking pattern emerges among state-of-the-art data-driven baselines: they all exhibit significant error accumulation in high-latitude regions, as highlighted by the red boxes. We attribute this common failure to their reliance on isotropic modeling assumptions. This approach inherently struggles with the severe projec-

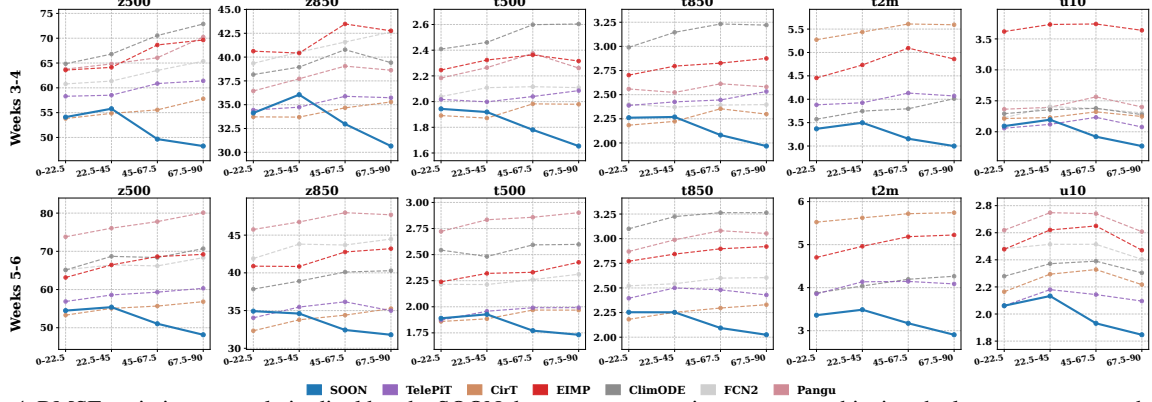


Figure 4. RMSE variation across latitudinal bands. SOON demonstrates superior accuracy, achieving the lowest errors near the poles.

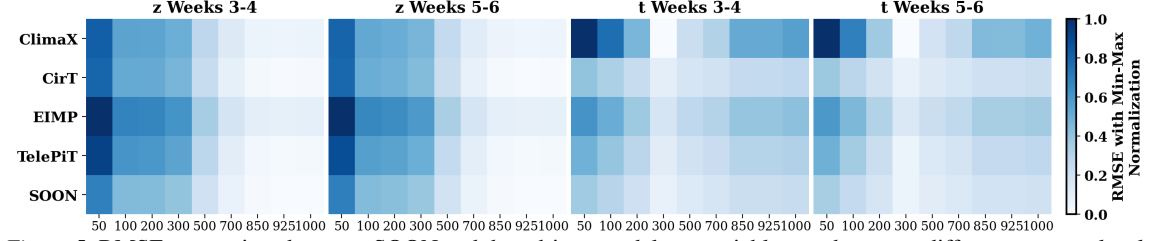


Figure 5. RMSE comparison between SOON and data-driven models on variable  $z$  and  $t$  across different pressure levels.

tion distortion near the poles. However, SOON maintains a low error profile globally. By adopting anisotropic embedding, SOON respects the distinct physical topology of latitudinal rings, immunizing predictions against high-latitude distortion. See more results in Appendix E.3.

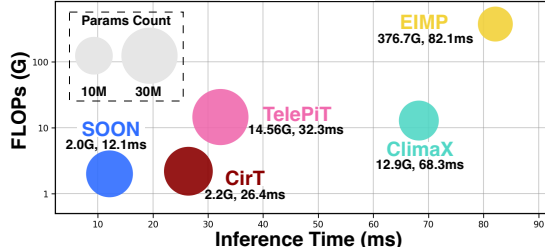


Figure 6. Efficiency analysis on the ERA5 dataset. Metrics are measured with batch size 1 and hidden dimension 256 for a fair comparison. Lower values indicate higher efficiency.

**Quantitative Latitudinal Analysis.** Figure 4 breaks down the RMSE across four latitudinal bands ranging from the equator ( $0^\circ$ ) to the pole ( $90^\circ$ ). A clear divergence in performance trends is observed: standard isotropic models exhibit a sharp upward error trend as latitude increases, confirming their vulnerability to grid convergence and projection distortion. In stark contrast, SOON demonstrates a unique inverse trend, where forecasting error often decreases or remains minimal in the polar region. This quantitative evidence reinforces that our anisotropic ring embedding not only resolves the singularity issue but effectively leverages the strong zonal continuity of polar dynamics, turning geometric constraints into a structural advantage.

**Performance Variation across Pressure Levels.** Figure 5 visualizes the normalized RMSE for variables ( $z$ ) and ( $t$ )

across 9 pressure levels. SOON consistently exhibits superior accuracy from the stratosphere to the near-surface. In contrast, baselines show distinct performance degradation, particularly in the upper atmosphere (50–200 hPa). This vertical consistency confirms that our anisotropic embedding and symmetric operator design effectively preserve the physical coherence of atmospheric profiles across all altitudes. See more visualizations in Appendix E.4. Additionally, we present daily forecasting performance within the bi-weekly horizon in Appendix E.5, and monthly forecasting performance over the full testing set in Appendix E.6.

**Efficiency Comparison.** Figure 6 highlights the efficiency of SOON. Our model substantially reduces computational burdens compared to existing baselines. Notably, SOON achieves an inference speedup of over  $2\times$  and  $5\times$  compared to CirT and Climax, respectively. This efficiency stems from our anisotropic design, replacing quadratic attention mechanisms with linear-complexity Zonal and Meridional operators, ensuring scalability for practical forecasting.

## 5. Conclusion and Future Work

This paper addresses the fundamental mismatch between existing isotropic baselines and anisotropic atmospheric dynamics in S2S forecasting. We propose SOON, a physics-aligned architecture that explicitly decouples zonal waves from meridional transport via anisotropic ring embedding and a symmetric Strang splitting scheme. Empirical results on ERA5 confirm that SOON establishes a new state-of-the-art in both accuracy and efficiency. We discuss the limitations of SOON in Appendix F. Future work will focus on integrating generative frameworks to quantify forecast uncertainty essential for chaotic S2S timescales.

## Impact Statements

This work contributes to global subseasonal-to-seasonal forecasting. We do not foresee any negative ethical consequences or societal impacts from it.

## References

Ba, J. L., Kiros, J. R., and Hinton, G. E. Layer normalization. *arXiv:1607.06450*, 2016.

Baker, H. F. Alternants and continuous groups. *Proceedings of The London Mathematical Society*, 1905.

Bi, K., Xie, L., Zhang, H., Chen, X., Gu, X., and Tian, Q. Accurate medium-range global weather forecasting with 3d neural networks. *Nature*, 2023.

Blanes, S. and Casas, F. *A concise introduction to geometric numerical integration*. CRC press, 2025.

Chen, K., Han, T., Gong, J., Bai, L., Ling, F., Luo, J.-J., Chen, X., Ma, L., Zhang, T., Su, R., et al. Fengwu: Pushing the skillful global medium-range weather forecast beyond 10 days lead. *arXiv:2304.02948*, 2023a.

Chen, L., Zhong, X., Zhang, F., Cheng, Y., Xu, Y., Qi, Y., and Li, H. Fuxi: a cascade machine learning forecasting system for 15-day global weather forecast. *npj Climate and Atmospheric Science*, 2023b.

Chen, L., Zhong, X., Li, H., Wu, J., Lu, B., Chen, D., Xie, S.-P., Wu, L., Chao, Q., Lin, C., et al. A machine learning model that outperforms conventional global subseasonal forecast models. *Nature Communications*, 2024.

Dauphin, Y. N., Fan, A., Auli, M., and Grangier, D. Language modeling with gated convolutional networks. *arXiv:1612.08083*, 2017.

Dosovitskiy, A. An image is worth 16x16 words: Transformers for image recognition at scale. *arXiv:2010.11929*, 2020.

Fang, Y., Miao, H., Liang, Y., Deng, L., Cui, Y., Zeng, X., Xia, Y., Zhao, Y., Pedersen, T. B., Jensen, C. S., Zhou, X., and Zheng, K. Unraveling spatio-temporal foundation models via the pipeline lens: A comprehensive review. *TKDE*, 2026.

Hairer, E., Hochbruck, M., Iserles, A., and Lubich, C. Geometric numerical integration. *Oberwolfach Reports*, 2006.

Harbola, S. and Coors, V. One dimensional convolutional neural network architectures for wind prediction. *Energy Conversion and Management*, 2019.

Hersbach, H., Bell, B., Berrisford, P., Hirahara, S., Horányi, A., Muñoz-Sabater, J., Nicolas, J., Peubey, C., Radu, R., Schepers, D., et al. The era5 global reanalysis. *Quarterly Journal of the Royal Meteorological Society*, 2020.

Hoskins, B. J. and Karoly, D. J. The steady linear response of a spherical atmosphere to thermal and orographic forcing. *Journal of Atmospheric Sciences*, 1981.

Lam, R., Sanchez-Gonzalez, A., Willson, M., Wirnsberger, P., Fortunato, M., Alet, F., Ravuri, S., Ewalds, T., Eaton-Rosen, Z., Hu, W., et al. Learning skillful medium-range global weather forecasting. *Science*, 2023.

Lang, S., Alexe, M., Chantry, M., Dramsch, J., Pinault, F., Raoult, B., Clare, M. C., Lessig, C., Maier-Gerber, M., Magnusson, L., et al. Aifs–ecmwf’s data-driven forecasting system. *arXiv:2406.01465*, 2024.

Li, G., Liu, X., Cao, S., Liang, H., Chen, M., Zhang, L., Zhang, J., Wang, J., Jin, M., Zheng, J., et al. Tianquant-climate: A subseasonal-to-seasonal global weather model via incorporate climatology state. *arXiv:2504.09940*, 2025.

Li, Z., Kovachki, N., Azizzadenesheli, K., Liu, B., Bhattacharya, K., Stuart, A., and Anandkumar, A. Fourier neural operator for parametric partial differential equations. *arXiv:2010.08895*, 2020.

Liu, Y., Zheng, Z., Cheng, J., Tsung, F., Zhao, D., Rong, Y., and Li, J. Cirt: Global subseasonal-to-seasonal forecasting with geometry-inspired transformer. In *ICLR*, 2025a.

Liu, Y., Zheng, Z., Rong, Y., Zhao, D., Cheng, H., and Li, J. Equivariant and invariant message passing for global subseasonal-to-seasonal forecasting. In *SIGKDD*, 2025b.

Lyu, T., Zhang, W., and Liu, H. Physics-informed teleconnection-aware transformer for global subseasonal-to-seasonal forecasting. In *SIGKDD*, 2026.

Mariotti, A., Ruti, P. M., and Rixen, M. Progress in subseasonal to seasonal prediction through a joint weather and climate community effort. *Npj Climate and Atmospheric Science*, 2018.

McLachlan, R. I. and Quispel, G. R. W. Splitting methods. *Acta Numerica*, 2002.

Molteni, F., Buizza, R., Palmer, T. N., and Petroliagis, T. The ecmwf ensemble prediction system: Methodology and validation. *Quarterly Journal of the Royal Meteorological Society*, 1996.

Mouatadid, S., Orenstein, P., Flaspholer, G., Cohen, J., Oprescu, M., Fraenkel, E., and Mackey, L. Adaptive

bias correction for improved subseasonal forecasting. *Nature Communications*, 2023.

Nathaniel, J., Qu, Y., Nguyen, T., Yu, S., Busecke, J., Grover, A., and Gentine, P. Chaosbench: A multi-channel, physics-based benchmark for subseasonal-to-seasonal climate prediction. In *NeurIPS*, 2024.

Nguyen, T., Brandstetter, J., Kapoor, A., Gupta, J. K., and Grover, A. Climax: A foundation model for weather and climate. *arXiv:2301.10343*, 2023.

Nguyen, T., Pham, T., Arcomano, T., Kotamarthi, V., Foster, I., Madireddy, S., and Grover, A. Omnicast: A masked latent diffusion model for weather forecasting across time scales. In *NeurIPS*, 2025.

Parseval, M.-A. Mémoire sur les séries et sur l'intégration complète d'une équation aux différences partielles linéaires du second ordre, à coefficients constants. *Mém. prés. par divers savants, Acad. des Sciences, Paris*, (1), 1806.

Pathak, J., Subramanian, S., Harrington, P., Raja, S., Chat-topadhyay, A., Mardani, M., Kurth, T., Hall, D., Li, Z., Azizzadenesheli, K., et al. Fourcastnet: A global data-driven high-resolution weather model using adaptive fourier neural operators. *arXiv:2202.11214*, 2022.

Peixoto, J. P. and Oort, A. H. Physics of climate. 1991.

Price, I., Sanchez-Gonzalez, A., Alet, F., Andersson, T. R., El-Kadi, A., Masters, D., Ewalds, T., Stott, J., Mohamed, S., Battaglia, P., et al. Probabilistic weather forecasting with machine learning. *Nature*, 2025.

Rasp, S., Dueben, P. D., Scher, S., Weyn, J. A., Mouatadid, S., and Thuerey, N. Weatherbench: a benchmark data set for data-driven weather forecasting. *Journal of Advances in Modeling Earth Systems*, 2020.

Rossby, C., Willett, H., Holmboe, M., Namias, J., Page, L., Allen, R., et al. Relation between variations in the intensity of the zonal circulation of the atmosphere and the displacements of the permanent centers of action atmosphere and the displacements of the permanent centers of action. *Journal of Marine Research*, 1939.

Saha, S., Moorthi, S., Wu, X., Wang, J., Nadiga, S., Tripp, P., Behringer, D., Hou, Y.-T., Chuang, H.-y., Iredell, M., et al. The ncep climate forecast system version 2. *Journal of Climate*, 2014.

Shi, X., Chen, Z., Wang, H., Yeung, D.-Y., Wong, W.-K., and Woo, W.-c. Convolutional lstm network: A machine learning approach for precipitation nowcasting. *NeurIPS*, 2015.

Strang, G. On the construction and comparison of difference schemes. *SIAM Journal on Numerical Analysis*, 1968.

Touvron, H., Cord, M., Sablayrolles, A., Synnaeve, G., and Jégou, H. Going deeper with image transformers. In *ICCV*, 2021.

Trotter, H. F. On the product of semi-groups of operators. *Proceedings of the American Mathematical Society*, 1959.

Vallis, G. K. *Atmospheric and oceanic fluid dynamics*. Cambridge University Press, 2017.

Vaswani, A., Shazeer, N., Parmar, N., Uszkoreit, J., Jones, L., Gomez, A. N., Kaiser, Ł., and Polosukhin, I. Attention is all you need. In *NeurIPS*, 2017.

Verma, Y., Heinonen, M., and Garg, V. Climode: Climate and weather forecasting with physics-informed neural odes. In *ICLR*, 2024.

Vitart, F., Ardilouze, C., Bonet, A., Brookshaw, A., Chen, M., Codorean, C., Déqué, M., Ferranti, L., Fucile, E., Fuentes, M., et al. The subseasonal to seasonal (s2s) prediction project database. *Bulletin of the American Meteorological Society*, 2017.

Wang, Y., Du, D., Hu, H., Liang, Z., and Liu, Y. Tsfool: Crafting highly-imperceptible adversarial time series through multi-objective attack. In *ECAI*, 2024.

White, C. J., Carlsen, H., Robertson, A. W., Klein, R. J., Lazo, J. K., Kumar, A., Vitart, F., Coughlan de Perez, E., Ray, A. J., Murray, V., et al. Potential applications of subseasonal-to-seasonal (s2s) predictions. *Meteorological Applications*, 2017.

Wu, T., Lu, Y., Fang, Y., Xin, X., Li, L., Li, W., Jie, W., Zhang, J., Liu, Y., Zhang, L., et al. The beijing climate center climate system model (bcc-csm): The main progress from cmip5 to cmip6. *Geoscientific Model Development*, 2019.

Zhang, B. and Sennrich, R. Root mean square layer normalization. *arXiv:1910.07467*, 2019.

Zheng, Z., Liu, Y., and Li, J. Mesh interpolation graph network for dynamic and spatially irregular global weather forecasting. *arXiv:2509.20911*, 2025.

Zhou, Z., Lyu, G., Huang, Y., Wang, Z., Jia, Z., and Yang, Z. Sdformer: Transformer with spectral filter and dynamic attention for multivariate time series long-term forecasting. In *IJCAI*, 2024.

Zhou, Z., Huang, Y., Wang, Y., Wu, Y., Kwok, J., and Liang, Y. Revitalizing canonical pre-alignment for irregular multivariate time series forecasting. In *AAAI*, 2026.

# Appendix (Supplementary Material)

SOON: Symmetric Orthogonal Operator Network for Global  
Subseasonal-to-Seasonal Climate Forecasting

## TABLE OF CONTENTS

---

<b>A Related Works</b>	<b>12</b>
A.1 Data-driven Weather Forecasting . . . . .	12
A.2 Data-driven S2S Forecasting . . . . .	12
<b>B Theoretical Model Complexity</b>	<b>12</b>
<b>C Theoretical Proofs</b>	<b>12</b>
C.1 Proof of Theorem 3.1: Local Truncation Error of SOON Block . . . . .	12
C.2 Proof of Proposition 3.2: Spectral Distortion of LayerNorm . . . . .	13
C.3 Proof of Proposition 3.3: Spectral Fidelity of RMSNorm . . . . .	14
<b>D Experimental Details</b>	<b>14</b>
D.1 Dataset . . . . .	14
D.2 Baselines . . . . .	15
D.3 Implementation Details . . . . .	16
<b>E Additional Results</b>	<b>16</b>
E.1 Performance w.r.t. the number of SOON blocks . . . . .	16
E.2 Spectral Energy Distribution Analysis . . . . .	16
E.3 Additional Global Visualizations . . . . .	17
E.4 Vertical Profile Analysis . . . . .	22
E.5 Daily Visualization and Temporal Stability . . . . .	22
E.6 Seasonal Robustness Analysis . . . . .	22
<b>F Limitations</b>	<b>24</b>

---

## A. Related Works

### A.1. Data-driven Weather Forecasting

Spatio-temporal data, together with time series data, are prevalent across various domains of daily life, among which weather data are closely related to human activities (Fang et al., 2026; Wang et al., 2024; Zhou et al., 2024). Recently, deep learning has emerged as a computationally efficient alternative to traditional Numerical Weather Prediction (NWP) systems (Vitart et al., 2017; White et al., 2017). While early works focused on regional tasks (Shi et al., 2015; Harbola & Coors, 2019), the release of ERA5 (Hersbach et al., 2020) has shifted focus to global forecasting. Foundational benchmarks (Rasp et al., 2020) paved the way for models that rival operational NWP systems (e.g., IFS) in the medium range. Prominent architectures include Adaptive Fourier Neural Operators (FourCastNet (Pathak et al., 2022)), Graph Neural Networks (GraphCast (Lam et al., 2023), AIFS (Lang et al., 2024)), and Transformers (PanguWeather (Bi et al., 2023), FengWu (Chen et al., 2023a), FuXi (Chen et al., 2023b)). Recent research also explores probabilistic forecasting via diffusion models (Price et al., 2025). However, the performance of these medium-range models often degrades at subseasonal scales due to the lack of physical constraints and error accumulation.

### A.2. Data-driven S2S Forecasting

Subseasonal-to-Seasonal (S2S) forecasting (2–6 weeks) remains a grand challenge due to chaotic atmospheric dynamics. While traditional dynamical models (e.g., ECMWF (Molteni et al., 1996)) face computational bottlenecks, recent global data-driven models have shown promise. ClimaX (Nguyen et al., 2023) adapts a vision foundation model for climate tasks via fine-tuning. FuXi-S2S (Chen et al., 2024) employs a cascade architecture to forecast daily averaged statistics. CirT (Liu et al., 2025a) introduces circular patching strategies to better handle spherical boundary conditions. EIMP (Liu et al., 2025b) leverages graph neural networks with rotation-equivariant message passing to model vector fields. TelePiT (Lyu et al., 2026) combines spherical harmonics with physics-informed neural ODEs to capture multi-scale teleconnections, while TianQuan-S2S (Li et al., 2025) further enhances predictability by incorporating climatology priors and noise injection. However, these approaches predominantly rely on isotropic modeling assumptions that neglect the distinct physical nature of zonal waves versus meridional transport, often suffering from high computational costs and error accumulation. In contrast, our proposed SOON introduces a physics-aligned anisotropic architecture that explicitly disentangles these dynamics, achieving superior computational efficiency and forecasting stability.

## B. Theoretical Model Complexity

Here, we provide the step-by-step derivation of the time complexity for both standard Transformers and SOON. For standard Transformer-based models (e.g., ClimaX (Nguyen et al., 2023), ViT (Dosovitskiy, 2020), CirT (Liu et al., 2025a)), the input grid  $H \times W$  is typically tokenized into  $T \propto HW$  patches. Consequently, the computational cost is dominated by the global self-attention mechanism, which scales as  $\mathcal{O}(T^2C)$ , and feed-forward networks scaling as  $\mathcal{O}(TC^2)$ . Substituting  $T$ , the total complexity becomes  $\mathcal{O}((HW)^2C + HWC^2) \approx \mathcal{O}(H^2W^2C)$ , exhibiting a quadratic dependency on both latitudinal ( $H$ ) and longitudinal ( $W$ ) resolutions. In contrast, SOON utilizes anisotropic embedding to compress the longitudinal dimension, resulting in a reduced sequence length of  $H$ . The computational burden of a single SOON block comprises three specific components: the Zonal Operator, which performs FFT and iFFT along the feature dimension with complexity  $\mathcal{O}(HC \log C)$ ; the Meridional Operator, which applies depthwise 1D convolution with kernel size  $k$  along the sequence length, costing  $\mathcal{O}(HCK)$ ; and the point-wise feed-forward networks, contributing  $\mathcal{O}(HC^2)$ . Summing these terms yields a total complexity of  $\mathcal{O}(H(C^2 + C \log C + CK))$ . This derivation explicitly demonstrates that the longitudinal width  $W$  does not factor into the backbone’s computational cost, confirming that SOON scales linearly with  $H$ .

## C. Theoretical Proofs

### C.1. Proof of Theorem 3.1: Local Truncation Error of SOON Block

**Theorem 3.1.** *Let  $\mathcal{L}_Z$  and  $\mathcal{L}_M$  denote the infinitesimal generators corresponding to the Zonal and Meridional operators, respectively. Let  $\mathcal{S}_{\text{SOON}}(\tau)$  denote the evolution operator of one SOON block approximating the exact dynamics  $e^{\tau(\mathcal{L}_Z + \mathcal{L}_M)}$ . By enforcing the symmetric composition  $\mathcal{Z} \circ \mathcal{M} \circ \mathcal{Z}$  (implemented as the Strang splitting  $e^{\frac{\tau}{2}\mathcal{L}_Z} e^{\tau\mathcal{L}_M} e^{\frac{\tau}{2}\mathcal{L}_Z}$ ), the local truncation error is of third order, i.e.,  $\|\mathcal{S}_{\text{SOON}}(\tau) - e^{\tau(\mathcal{L}_Z + \mathcal{L}_M)}\| = \mathcal{O}(\tau^3)$ , which is strictly superior to the  $\mathcal{O}(\tau^2)$  error of standard sequential stacking based on the Lie-Trotter splitting (Trotter, 1959).*

*Proof.* Let  $\mathcal{L}_{\text{total}} = \mathcal{L}_Z + \mathcal{L}_M$ . The exact evolution operator is  $\mathcal{E}(\tau) = \exp(\tau\mathcal{L}_{\text{total}})$ . We analyze the local truncation error

by comparing the logarithms of the numerical and exact operators via the Baker–Campbell–Hausdorff (BCH) formula.

**Sequential Stacking (Lie-Trotter Splitting).** Standard architectures approximate the flow as  $\mathcal{S}_{\text{Seq}}(\tau) = e^{\tau\mathcal{L}_M}e^{\tau\mathcal{L}_Z}$ . Using the BCH expansion  $\ln(e^X e^Y) = X + Y + \frac{1}{2}[X, Y] + \mathcal{O}(\|X, Y\|^3)$  with  $X = \tau\mathcal{L}_M$  and  $Y = \tau\mathcal{L}_Z$ :

$$\begin{aligned}\ln(\mathcal{S}_{\text{Seq}}(\tau)) &= \tau(\mathcal{L}_M + \mathcal{L}_Z) + \frac{\tau^2}{2}[\mathcal{L}_M, \mathcal{L}_Z] + \mathcal{O}(\tau^3) \\ &= \ln(\mathcal{E}(\tau)) + \frac{\tau^2}{2}[\mathcal{L}_M, \mathcal{L}_Z] + \mathcal{O}(\tau^3).\end{aligned}\tag{11}$$

Since  $[\mathcal{L}_M, \mathcal{L}_Z] \neq 0$  in general, the dominant local error term is  $\mathcal{O}(\tau^2)$ .

**SOON Block (Symmetric Composition  $\mathcal{Z} \circ \mathcal{M} \circ \mathcal{Z}$ ).** The SOON block implements the symmetric composition  $\mathcal{S}_{\text{SOON}}(\tau) = e^{\frac{\tau}{2}\mathcal{L}_Z}e^{\tau\mathcal{L}_M}e^{\frac{\tau}{2}\mathcal{L}_Z}$  corresponding to  $\mathcal{Z} \circ \mathcal{M} \circ \mathcal{Z}$ . Applying the symmetric BCH formula (Hairer et al., 2006) for  $\ln(e^{X/2}e^Y e^{X/2})$ :

$$\ln(e^{\frac{X}{2}}e^Y e^{\frac{X}{2}}) = X + Y + \frac{1}{24}[Y, [Y, X]] - \frac{1}{12}[X, [X, Y]] + \mathcal{O}(\|X, Y\|^4).\tag{12}$$

Substituting  $X = \tau\mathcal{L}_Z$  and  $Y = \tau\mathcal{L}_M$  (both  $\mathcal{O}(\tau)$ ):

$$\begin{aligned}\ln(\mathcal{S}_{\text{SOON}}(\tau)) &= \tau(\mathcal{L}_Z + \mathcal{L}_M) + \frac{\tau^3}{24}[\mathcal{L}_M, [\mathcal{L}_M, \mathcal{L}_Z]] - \frac{\tau^3}{12}[\mathcal{L}_Z, [\mathcal{L}_Z, \mathcal{L}_M]] + \mathcal{O}(\tau^4) \\ &= \ln(\mathcal{E}(\tau)) + \mathcal{O}(\tau^3).\end{aligned}\tag{13}$$

Crucially, the  $\mathcal{O}(\tau^2)$  commutator term  $[\mathcal{L}_Z, \mathcal{L}_M]$  vanishes due to the symmetry of the composition  $\mathcal{Z} \circ \mathcal{M} \circ \mathcal{Z}$ .

**Error Bound.** For sufficiently small  $\tau$  and under standard regularity assumptions on  $\mathcal{L}_Z, \mathcal{L}_M$  (e.g., generating analytic semigroups on a Banach space), the exponential map satisfies  $\|e^A - e^B\| \leq C\|A - B\|$  for some constant  $C > 0$  independent of  $\tau$  (Hairer et al., 2006). Setting  $A = \ln(\mathcal{S}_{\text{SOON}}(\tau))$  and  $B = \tau\mathcal{L}_{\text{total}}$ , we obtain:

$$\|\mathcal{S}_{\text{SOON}}(\tau) - \mathcal{E}(\tau)\| \leq C\|\ln(\mathcal{S}_{\text{SOON}}(\tau)) - \ln(\mathcal{E}(\tau))\| = \mathcal{O}(\tau^3).\tag{14}$$

Thus the SOON block achieves third-order local truncation error, strictly superior to the second-order local error of sequential stacking in prior global S2S forecasting works (Liu et al., 2025a;b; Lyu et al., 2026; Li et al., 2025).  $\square$

*Remark C.1 (Significance in S2S Forecasting).* The third-order local truncation error ( $\mathcal{O}(\tau^3)$ ) of SOON yields second-order global accuracy ( $\mathcal{O}(\tau^2)$ ), whereas Lie-Trotter splitting yields only first-order global accuracy ( $\mathcal{O}(\tau)$ ). For Subseasonal-to-Seasonal forecasting over total time  $T$  with step size  $\tau$  (requiring  $N = T/\tau$  steps), the accumulated global error for Lie-Trotter splitting scales as  $N \cdot \mathcal{O}(\tau^2) = \mathcal{O}(\tau)$ , while for SOON it scales as  $N \cdot \mathcal{O}(\tau^3) = \mathcal{O}(\tau^2)$ . This quadratic reduction in global error significantly delays numerical divergence from the true atmospheric manifold, which is critical for capturing chaotic dynamics and preserving slow-varying climatic patterns (e.g., MJO) deep into the predictability desert.

## C.2. Proof of Proposition 3.2: Spectral Distortion of LayerNorm

**Proposition 3.2.** Let  $\mathbf{z} \in \mathbb{R}^C$  be the latent representation of a latitudinal ring token in  $\mathbf{E}^{(0)}$  and let  $\hat{\mathbf{z}} = \mathcal{F}(\mathbf{z})$  be its discrete Fourier spectrum. LayerNorm introduces spectral distortion by eliminating the zero-frequency component (background energy), i.e.,  $|\mathcal{F}(\text{LayerNorm}(\mathbf{z}))_0| \equiv 0$ , where  $\mathcal{F}(\cdot)_0$  represents the 0-th frequency component of the DFT.

*Proof.* Let  $\mathbf{z} = [z_0, \dots, z_{C-1}]^\top \in \mathbb{R}^C$ . The Discrete Fourier Transform (DFT) is defined as  $\hat{z}_k = \sum_{n=0}^{C-1} z_n e^{-i2\pi kn/C}$ , where  $k = 0$  corresponds to the zero-frequency (DC) component. Layer Normalization centers the input via  $\mathbf{z}' = \mathbf{z} - \mu\mathbf{1}$ , where  $\mu = \frac{1}{C} \sum_{n=0}^{C-1} z_n$  is the mean value. By the linearity of the DFT operator  $\mathcal{F}$ , the zero-frequency component of the centered signal is:

$$\mathcal{F}(\mathbf{z}')_0 = \sum_{n=0}^{C-1} (z_n - \mu) = \sum_{n=0}^{C-1} z_n - C \cdot \left( \frac{1}{C} \sum_{n=0}^{C-1} z_n \right) = \hat{z}_0 - \hat{z}_0 = 0.\tag{15}$$

The subsequent scaling by standard deviation  $\sigma$  in LayerNorm ( $\frac{\mathbf{z}'}{\sigma}$ ) involves multiplication by a scalar, which does not alter the zero value at  $k = 0$ . Thus, LayerNorm acts as a hard high-pass filter that strictly removes the DC component  $\hat{z}_0$ , which represents the background energy state of the atmospheric field.  $\square$

### C.3. Proof of Proposition 3.3: Spectral Fidelity of RMSNorm

**Proposition 3.3.** *RMSNorm preserves the phase angles  $\arg(\mathcal{F}(\text{RMSN}(\mathbf{z})))_k = \arg(\hat{\mathbf{z}}_k)$  for all wave numbers  $k$ .*

*Proof.* RMSNorm applies a multiplicative scaling:  $\text{RMSN}(\mathbf{z}) = \lambda \mathbf{z}$ , where  $\lambda = (\frac{1}{C} \sum_{n=0}^{C-1} z_n^2)^{-1/2}$ . Since the energy must be non-negative,  $\lambda$  is a strictly positive real scalar ( $\lambda \in \mathbb{R}^+$ ). To analyze its spectral effect, we first invoke Parseval's Theorem (Parseval, 1806) to relate spatial-domain energy to spectral-domain energy.

**Derivation of Parseval's Identity.** Using the inverse DFT definition  $z_n = \frac{1}{C} \sum_{k=0}^{C-1} \hat{z}_k e^{i \frac{2\pi k n}{C}}$ :

$$\begin{aligned} \sum_{n=0}^{C-1} z_n^2 &= \sum_{n=0}^{C-1} z_n z_n^* = \sum_{n=0}^{C-1} \left( \frac{1}{C} \sum_{k=0}^{C-1} \hat{z}_k e^{i \frac{2\pi k n}{C}} \right) \left( \frac{1}{C} \sum_{k'=0}^{C-1} \hat{z}_{k'}^* e^{-i \frac{2\pi k' n}{C}} \right) \\ &= \frac{1}{C^2} \sum_{k=0}^{C-1} \sum_{k'=0}^{C-1} \underbrace{\hat{z}_k \hat{z}_{k'}^*}_{C \cdot \delta_{k,k'}} \underbrace{\sum_{n=0}^{C-1} e^{i \frac{2\pi (k-k') n}{C}}}_{\sum_{n=0}^{C-1} 1} = \frac{1}{C} \sum_{k=0}^{C-1} |\hat{z}_k|^2. \end{aligned} \quad (16)$$

This establishes that the total spatial energy is proportional to the total spectral energy. Substituting this into the RMSNorm scaling factor:

$$\lambda = \left( \frac{1}{C} \sum_{n=0}^{C-1} z_n^2 \right)^{-1/2} = \left( \frac{1}{C} \sum_{k=0}^{C-1} |\hat{z}_k|^2 \right)^{-1/2}. \quad (17)$$

The spectral representation of the normalized signal is given by the linearity of the Fourier transform:

$$\mathcal{F}(\text{RMSN}(\mathbf{z}))_k = \mathcal{F}(\lambda \mathbf{z})_k = \lambda \hat{z}_k. \quad (18)$$

Since  $\lambda$  is a positive real number, it affects only the magnitude of the complex spectral coefficients  $\hat{z}_k$ , but not their argument (phase angle). Therefore, for all wavenumbers  $k$ :

$$\arg(\mathcal{F}(\text{RMSN}(\mathbf{z})))_k = \arg(\lambda \hat{z}_k) = \arg(\hat{z}_k). \quad (19)$$

Furthermore, the relative spectral energy distribution is preserved:

$$\frac{|\mathcal{F}(\text{RMSN}(\mathbf{z}))_k|^2}{|\mathcal{F}(\text{RMSN}(\mathbf{z}))_{k'}|^2} = \frac{\lambda^2 |\hat{z}_k|^2}{\lambda^2 |\hat{z}_{k'}|^2} = \frac{|\hat{z}_k|^2}{|\hat{z}_{k'}|^2}, \quad \forall k, k'. \quad (20)$$

Critically, unlike LayerNorm, the zero-frequency component is preserved with non-zero magnitude ( $|\mathcal{F}(\text{RMSN}(\mathbf{z}))_0| = \lambda |\hat{z}_0| > 0$  when  $\hat{z}_0 \neq 0$ ), maintaining the background energy state essential for geostrophic balance.  $\square$

**Remark C.2 (Physical Implication for S2S Forecasting).** In atmospheric dynamics, the zero-frequency component ( $\hat{z}_0$ ) corresponds to the planetary background flow energy (e.g., mean zonal kinetic energy), while higher wavenumbers represent eddy energy. LayerNorm's elimination of the background energy disrupts the energy partitioning between mean flow and transient eddies, violating fundamental conservation principles. RMSNorm's uniform spectral scaling preserves both the phase structure and relative energy distribution, including the critical background energy state, ensuring physically consistent energy cascades during long-horizon integration. This spectral fidelity prevents artificial energy leakage between scales, which is essential for maintaining correct amplitude evolution of planetary waves and mitigating forecast drift in the predictability desert.

## D. Experimental Details

### D.1. Dataset

We evaluate SOON on the ERA5 reanalysis dataset (Hersbach et al., 2020), which provides a comprehensive record of global atmospheric conditions. To construct the training and evaluation data for our S2S forecasting task, we downsample the original  $0.25^\circ$  ERA5 data to a coarser resolution of  $1.5^\circ \times 1.5^\circ$  by sub-sampling grid points that align with the target grid. Specifically, we extract coordinates  $(\varphi, \lambda)$  on the latitude-longitude domain  $\Omega = [-90^\circ, 90^\circ] \times [-180^\circ, 180^\circ]$ , where

$\varphi \in \{-90^\circ, -88.5^\circ, \dots, 90^\circ\}$  and  $\lambda \in \{-180^\circ, -178.5^\circ, \dots, 178.5^\circ\}$ , resulting in a spatial resolution of  $121 \times 240$ . This regridding strategy ensures that our input data structure is consistent with the outputs of baseline models such as PanguWeather (Bi et al., 2023) and FourCastNetV2 (Pathak et al., 2022) when evaluated at this resolution. We select a set of 63 variables critical for capturing atmospheric dynamics, covering the time period from 1979 to 2018 with a temporal resolution of 1 day (daily averages). A detailed summary of the dataset configuration is provided in Table 3.

Table 3. Detailed configuration of the ERA5 dataset used in this work.

Category	Variable Name	Symbol	Levels	Resolution	Lat-Lon Range	Time
Pressure Level	Geopotential	$z$	10	$1.5^\circ$	$-90^\circ\text{S} 180^\circ\text{W} \sim 90^\circ\text{N} 180^\circ\text{E}$	1979 ~ 2018
	Specific Humidity	$q$	10	$1.5^\circ$	$-90^\circ\text{S} 180^\circ\text{W} \sim 90^\circ\text{N} 180^\circ\text{E}$	1979 ~ 2018
	Temperature	$t$	10	$1.5^\circ$	$-90^\circ\text{S} 180^\circ\text{W} \sim 90^\circ\text{N} 180^\circ\text{E}$	1979 ~ 2018
	U Component of Wind	$u$	10	$1.5^\circ$	$-90^\circ\text{S} 180^\circ\text{W} \sim 90^\circ\text{N} 180^\circ\text{E}$	1979 ~ 2018
	V Component of Wind	$v$	10	$1.5^\circ$	$-90^\circ\text{S} 180^\circ\text{W} \sim 90^\circ\text{N} 180^\circ\text{E}$	1979 ~ 2018
	Vertical Velocity	$w$	10	$1.5^\circ$	$-90^\circ\text{S} 180^\circ\text{W} \sim 90^\circ\text{N} 180^\circ\text{E}$	1979 ~ 2018
Single Level	2 Metre Temperature	$t2m$	1	$1.5^\circ$	$-90^\circ\text{S} 180^\circ\text{W} \sim 90^\circ\text{N} 180^\circ\text{E}$	1979 ~ 2018
	10 Metre U Wind	$u10$	1	$1.5^\circ$	$-90^\circ\text{S} 180^\circ\text{W} \sim 90^\circ\text{N} 180^\circ\text{E}$	1979 ~ 2018
	10 Metre V Wind	$v10$	1	$1.5^\circ$	$-90^\circ\text{S} 180^\circ\text{W} \sim 90^\circ\text{N} 180^\circ\text{E}$	1979 ~ 2018

## D.2. Baselines

To rigorously evaluate the performance of SOON, we benchmark it against a comprehensive set of baseline models:

**Operational Forecasting Systems.** These established numerical weather prediction (NWP) systems represent the current gold standard in operational meteorological forecasting.

- **CMA:** The China Meteorological Administration implements the Beijing Climate Center’s fully-coupled BCC-CSM2-HR model (Wu et al., 2019), providing operational forecasts with a 60-day lead time.
- **NCEP:** The National Centers for Environmental Prediction deploys the Climate Forecast System version 2 (CFSv2) (Saha et al., 2014) to generate daily control forecasts extending to a 45-day prediction window.
- **ECMWF:** The European Centre for Medium-Range Weather Forecasts employs the Integrated Forecasting System (IFS) (Molteni et al., 1996). We utilize the control forecasts from cycle 47r3, which are widely regarded as the most skillful operational baseline for S2S prediction.

**Data-Driven Models.** We compare against both pre-trained foundation models and models trained from scratch.

- **PanguWeather (Bi et al., 2023):** A 3D Earth-specific Transformer that tokenizes pressure-level and surface data separately, trained using a hierarchical temporal aggregation strategy. We use the API <https://github.com/ecmwf-lab/ai-models> to perform inference.
- **FourCastNetV2 (FCN2) (Pathak et al., 2022):** An iterative model based on Vision Transformers that incorporates Adaptive Fourier Neural Operators (AFNO) for efficient spatial token mixing. We use the API <https://github.com/ecmwf-lab/ai-models> to perform inference.
- **Transformer (Vaswani et al., 2017):** The standard self-attention architecture adapted for global grid inputs, serving as a fundamental baseline for sequence modeling capability.
- **FNO (Li et al., 2020):** The Fourier Neural Operator, which learns resolution-invariant operators by parameterizing the integral kernel in the frequency domain, adapted here for global forecasting.
- **ViT (Dosovitskiy, 2020):** The standard Vision Transformer employing a naive grid patching strategy, treating global weather fields as flat images without specific geometric adaptations.

- **ClimaX (Nguyen et al., 2023):** A foundation model for weather and climate using a Vision Transformer backbone with variable-specific tokenization and aggregation, retrained on our dataset.
- **ClimODE (Verma et al., 2024):** A physics-informed approach that models atmospheric dynamics using Neural Ordinary Differential Equations (ODEs) to capture continuous-time evolution.
- **CirT (Liu et al., 2025a):** A Transformer-based model designed for S2S forecasting that introduces circular patching and frequency-domain mixing to address spherical boundary conditions.
- **EIMP (Liu et al., 2025b):** A graph-based model utilizing equivariant and invariant message passing to strictly enforce rotational symmetries on spherical grids.
- **TelePiT (Lyu et al., 2026):** A physics-informed Transformer that integrates spherical harmonic embeddings with neural ODEs to explicitly capture multi-scale teleconnections.

### D.3. Implementation Details

The SOON model is implemented using PyTorch 2.3.1 and trained on 8 NVIDIA GPUs via Distributed Data Parallel (DDP) with mixed precision (FP16), while FFT operations within the Zonal Operator are forced to FP32 to ensure numerical stability. We utilize an anisotropic embedding kernel size of  $(1, 240)$  and a meridional spatial kernel size of  $k = 7$ . The model is trained for 20 epochs with a global batch size of 256 using the AdamW optimizer (weight decay  $10^{-5}$ ,  $\epsilon = 10^{-8}$ ) and gradient clipping at 1.0. The learning rate follows a cosine annealing schedule, decaying from a peak of  $10^{-3}$  to  $10^{-4}$ . To determine the optimal architecture, we conducted a grid search on the validation set over the following hyperparameter spaces: embedding dimension  $C \in \{128, 192, 256, 384, 512\}$ , network depth  $L \in \{4, 5, 6, 7, 8, 9\}$ , decoder depth  $\in \{1, 2, 3\}$ , learning rate  $\in \{5 \times 10^{-4}, 1 \times 10^{-3}, 5 \times 10^{-3}\}$ , MLP ratio  $\in \{2.0, 4.0, 6.0\}$ , and dropout rates  $\in \{0.0, 0.1, 0.2\}$ . The final selected configuration is  $C = 256$ ,  $L = 7$ , decoder depth 1, learning rate  $10^{-3}$ , MLP ratio 4.0, and dropout 0.1, resulting in a parameter count of approximately 16.58M.

We have also conducted comprehensive ablation studies as aforementioned in Section 4.3. The variants are implemented as follows:

1. Variant without Anisotropic Embedding (w/o AE): We replace the proposed  $(1, W)$  anisotropic convolution with a standard isotropic patch embedding of size  $4 \times 4$ , which flattens the input into a generic token sequence devoid of latitudinal ring topology.
2. Variant without Zonal Operator (w/o ZO): We remove the spectral mechanism and replace the  $\mathcal{Z} \circ \mathcal{M} \circ \mathcal{Z}$  symmetric structure with stacked Meridional operators ( $\mathcal{M} \circ \mathcal{M}$ ) to maintain model capacity.
3. Variant without Meridional Operator (w/o MO): We replace the spatial operator with a double Zonal structure ( $\mathcal{Z} \circ \mathcal{Z}$ ).
4. Variant with unshared-weight Zonal Operator (w/ unshared ZO): We define two independent Zonal Operators,  $\mathcal{Z}_1$  and  $\mathcal{Z}_2$ , resulting in an asymmetric structure  $\mathcal{Z}_1 \circ \mathcal{M} \circ \mathcal{Z}_2$ .
5. Variant with LayerNorm (w/ LN): We replace all RMSNorm layers with standard Layer Normalization to evaluate the impact of mean-centering on long-term stability.

## E. Additional Results

### E.1. Performance w.r.t. the number of SOON blocks

We evaluate the impact of network depth by varying the number of SOON blocks  $L \in \{4, 5, 6, 7, 8, 9\}$ . As can be seen from Figure 7, forecasting performance consistently improves as depth increases, peaking at  $L = 7$  where RMSE reaches a minimum for key variables. Increasing the depth further yields diminishing returns or slight degradation. Thus, we select  $L = 7$  to balance accuracy and computational efficiency.

### E.2. Spectral Energy Distribution Analysis

We further assess spectral energy distribution accuracy using SpecRes (Lyu et al., 2026) across all pressure levels for the prognostic variables  $z, t, u$ , and  $v$  under weeks 3–4 and weeks 5–6 forecasts. SpecRes quantifies the root of the expected

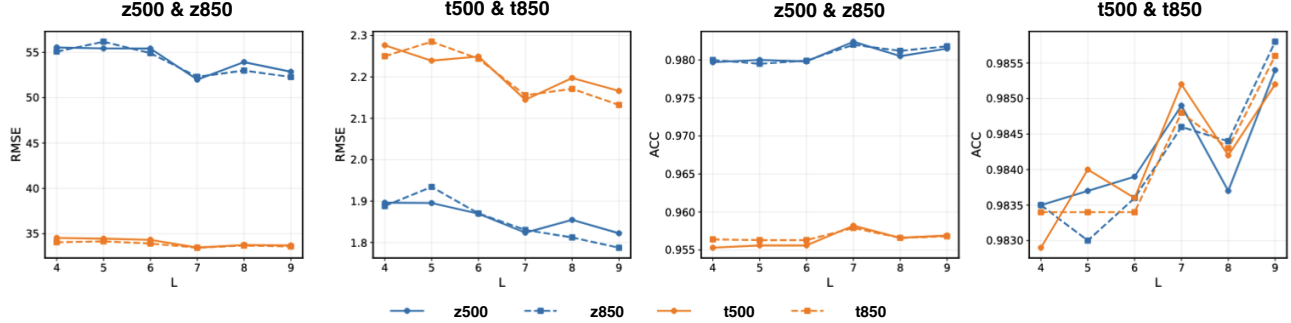


Figure 7. RMSE and ACC variations across different numbers of SOON blocks ( $L$ ) indicate that  $L = 7$  achieves the best trade-off between performance and model complexity.

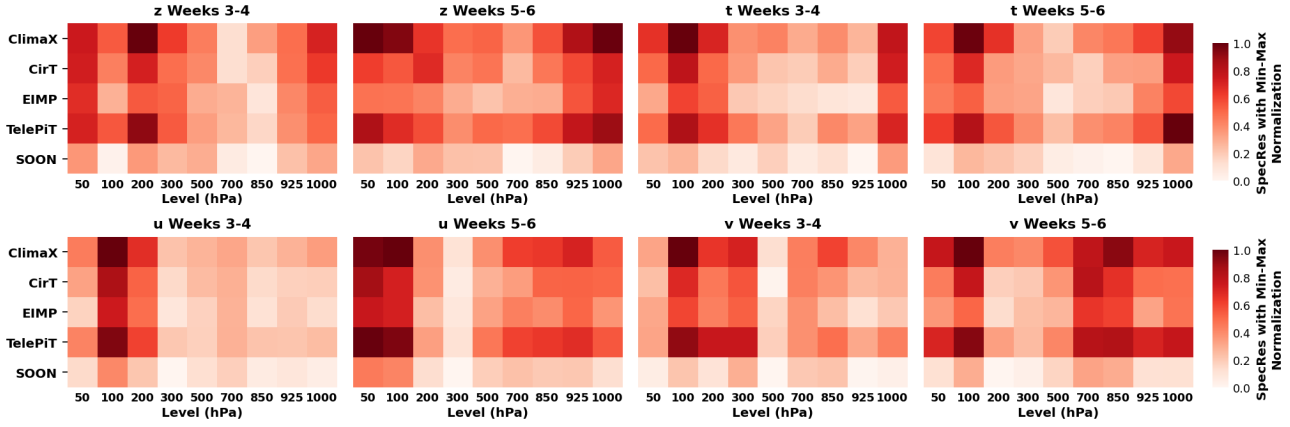


Figure 8. SpecRes comparison across pressure levels. SpecRes measures spectral energy distribution accuracy (lower is better; lighter colors indicate smaller values).

squared residual in the spectral domain, i.e.,  $\text{SpecRes} = \sqrt{\mathbb{E}_k[(\hat{S}'(k) - S'(k))^2]}$ , where  $\hat{S}'(k)$  and  $S'(k)$  denote the normalized power spectra of prediction and target, respectively. Therefore, lower SpecRes values indicate a more accurate preservation of spectral energy distribution, especially for high-frequency wavenumbers. As shown in Figure 8, SOON consistently exhibits substantially lower SpecRes values than all competing models over nearly all vertical levels, indicating a more faithful preservation of spectral energy distribution during long-horizon integration. This empirical observation aligns with our theoretical analysis: compared with mean-centering normalization, RMSNorm better preserves phase stability and background energy, thereby mitigating long-term spectral drift and improving spectral fidelity.

### E.3. Additional Global Visualizations

We provide expanded global error maps to visually assess spatial performance distributions across different variables and lead times. Figure 9 through Figure 15 display the RMSE distributions for  $t850$ ,  $t500$ ,  $z500$ , and  $z850$  during weeks 3–4 and weeks 5–6. Consistent with the findings in the main text, SOON exhibits deep blue patterns globally, indicating low error. A recurrent weakness in baseline models is the high error accumulation in polar regions (red/orange zones), caused by the projection distortion of isotropic kernels on the sphere. SOON effectively eliminates these artifacts, maintaining high accuracy in both the tropics and high latitudes. Furthermore, even as the forecast horizon extends to weeks 5–6, SOON preserves structural details better than competitors, which tend to produce overly smooth or erroneous fields.

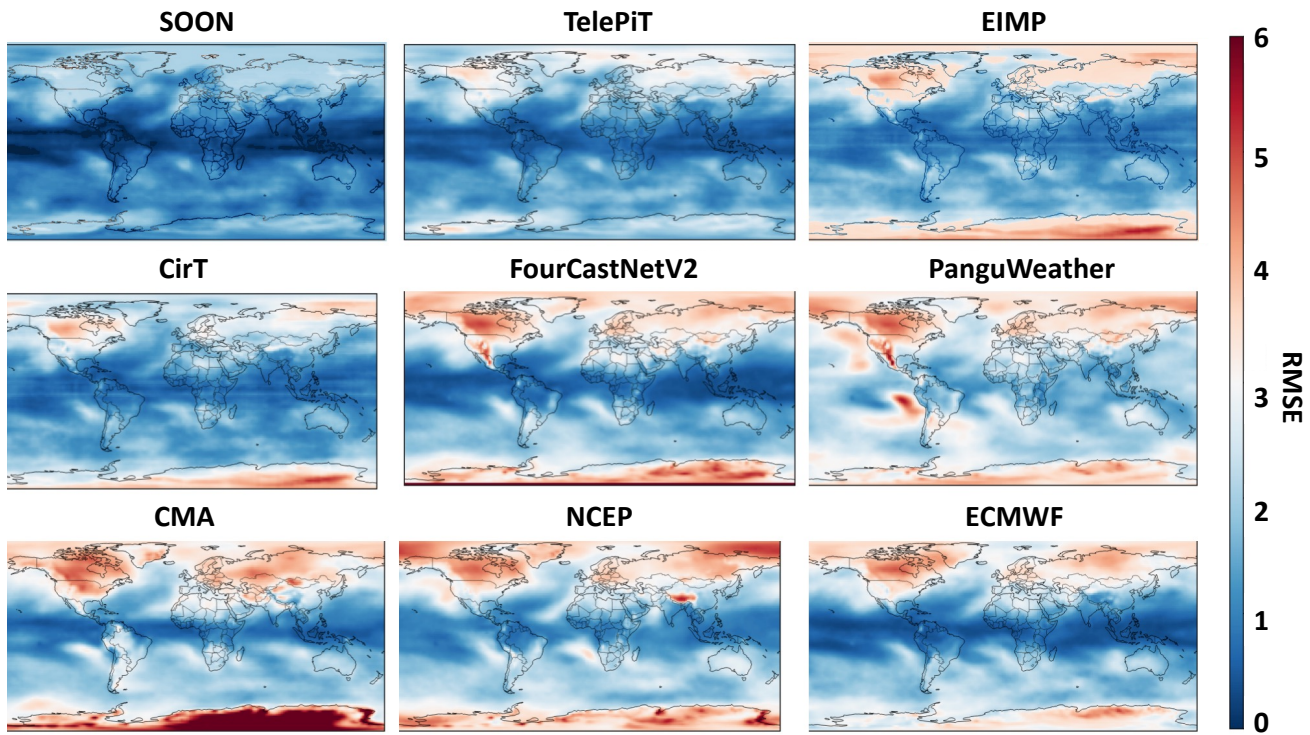


Figure 9. Global RMSE distribution for  $t850$  at weeks 5–6 lead time.

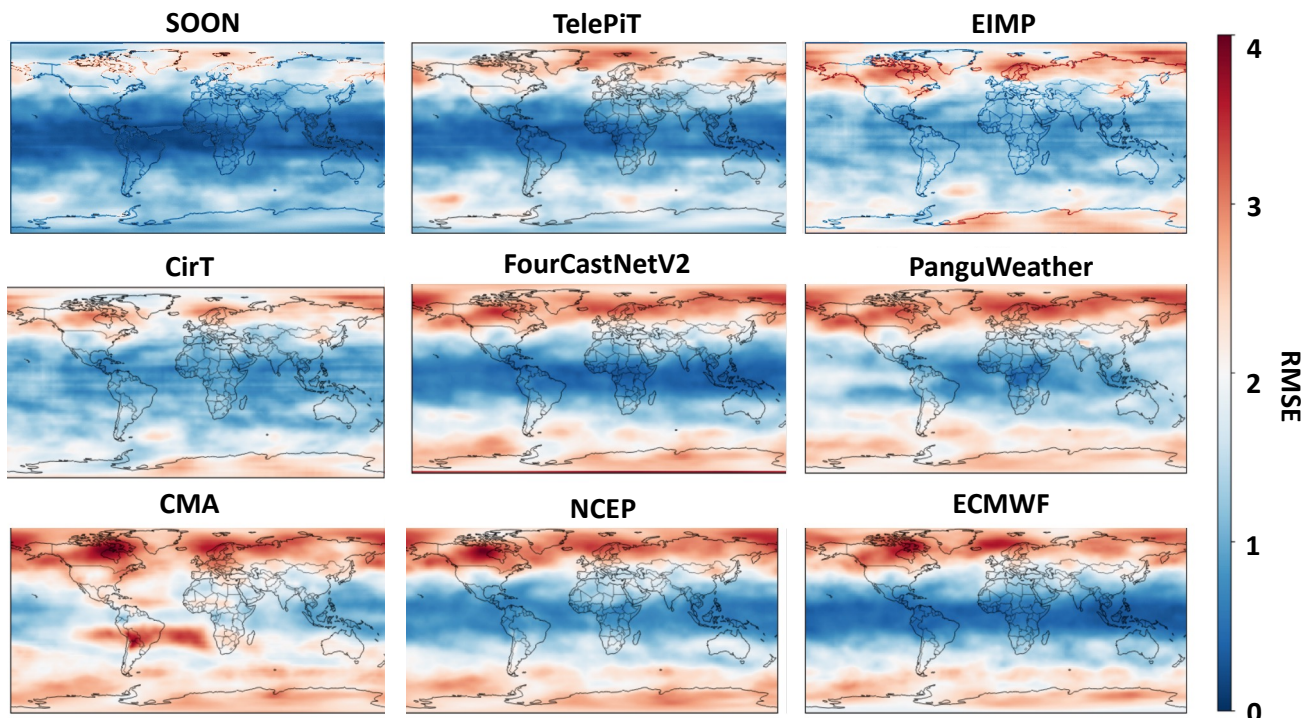


Figure 10. Global RMSE distribution for  $t500$  at weeks 3–4 lead time.

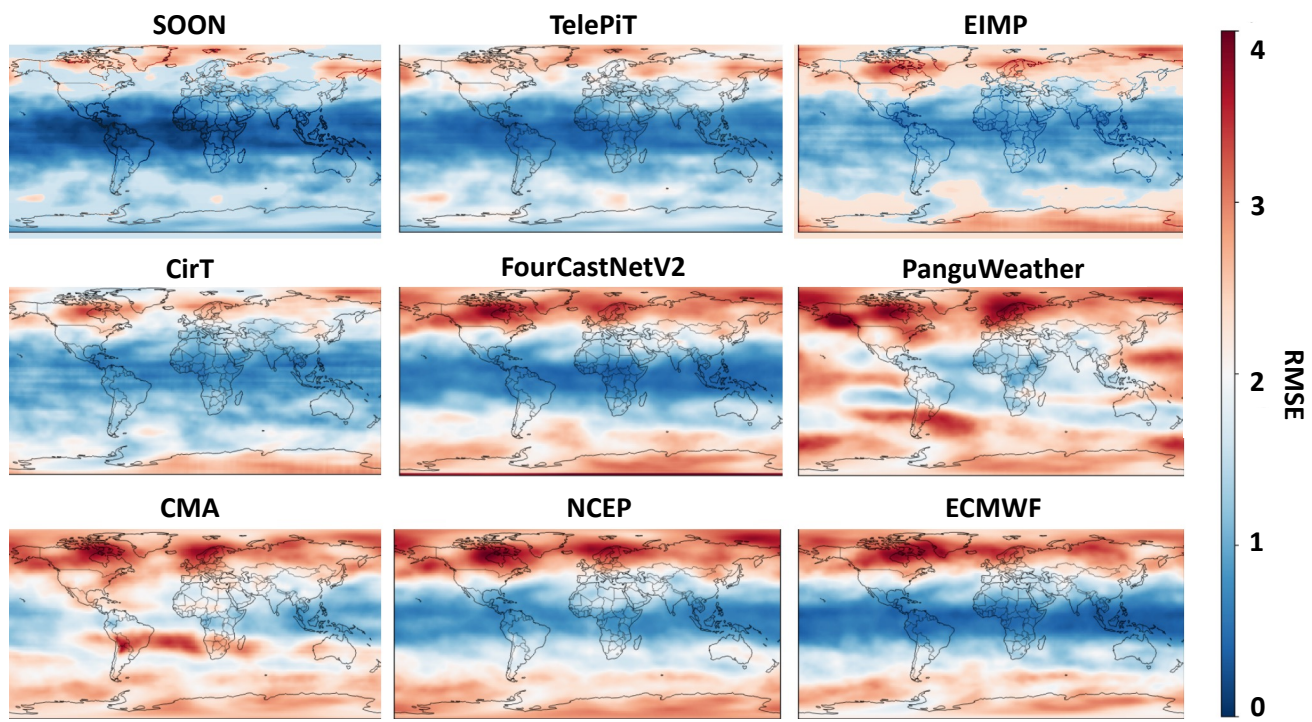


Figure 11. Global RMSE distribution for  $t500$  at weeks 5–6 lead time.

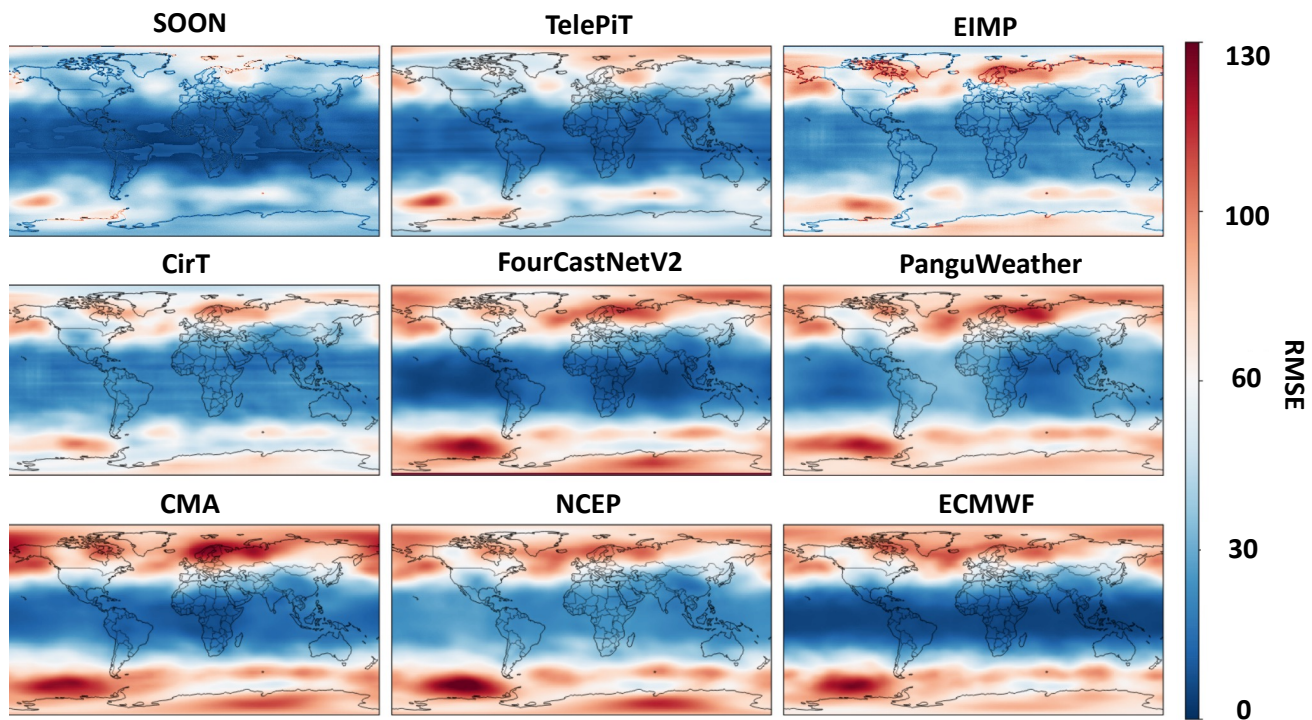


Figure 12. Global RMSE distribution for  $z500$  at weeks 3–4 lead time.

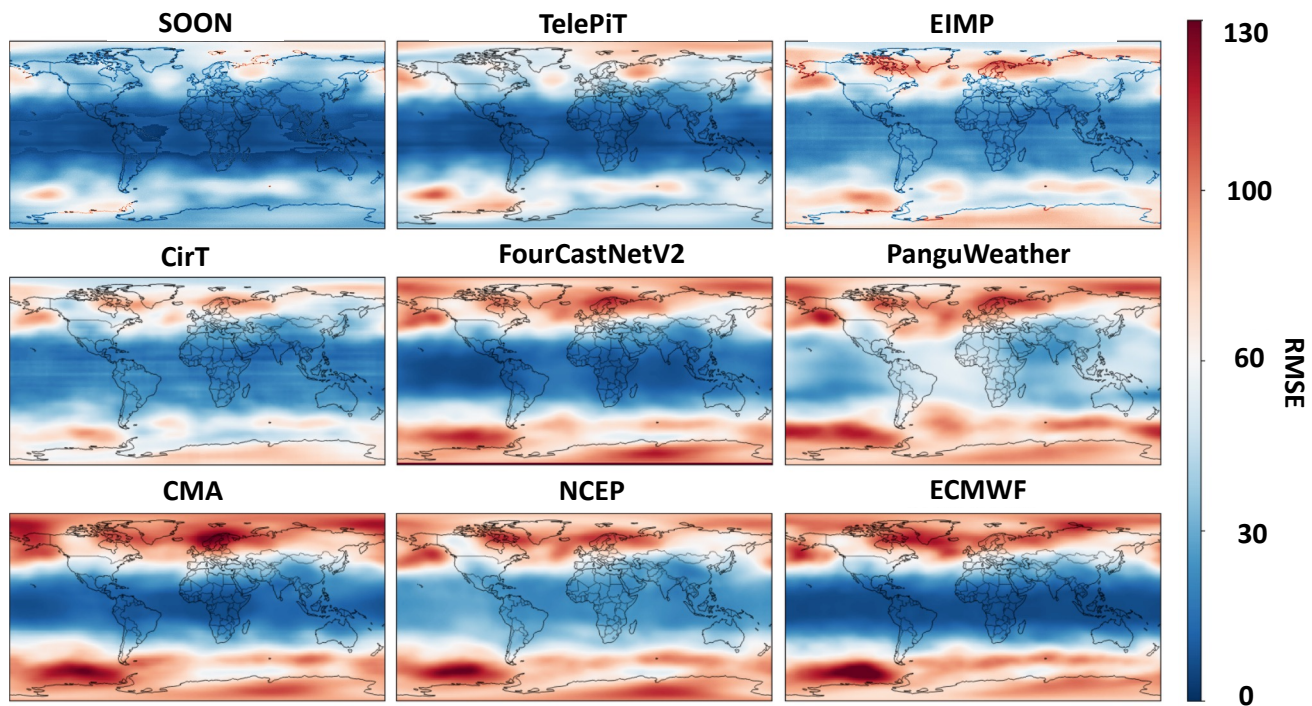


Figure 13. Global RMSE distribution for  $z500$  at weeks 5–6 lead time.

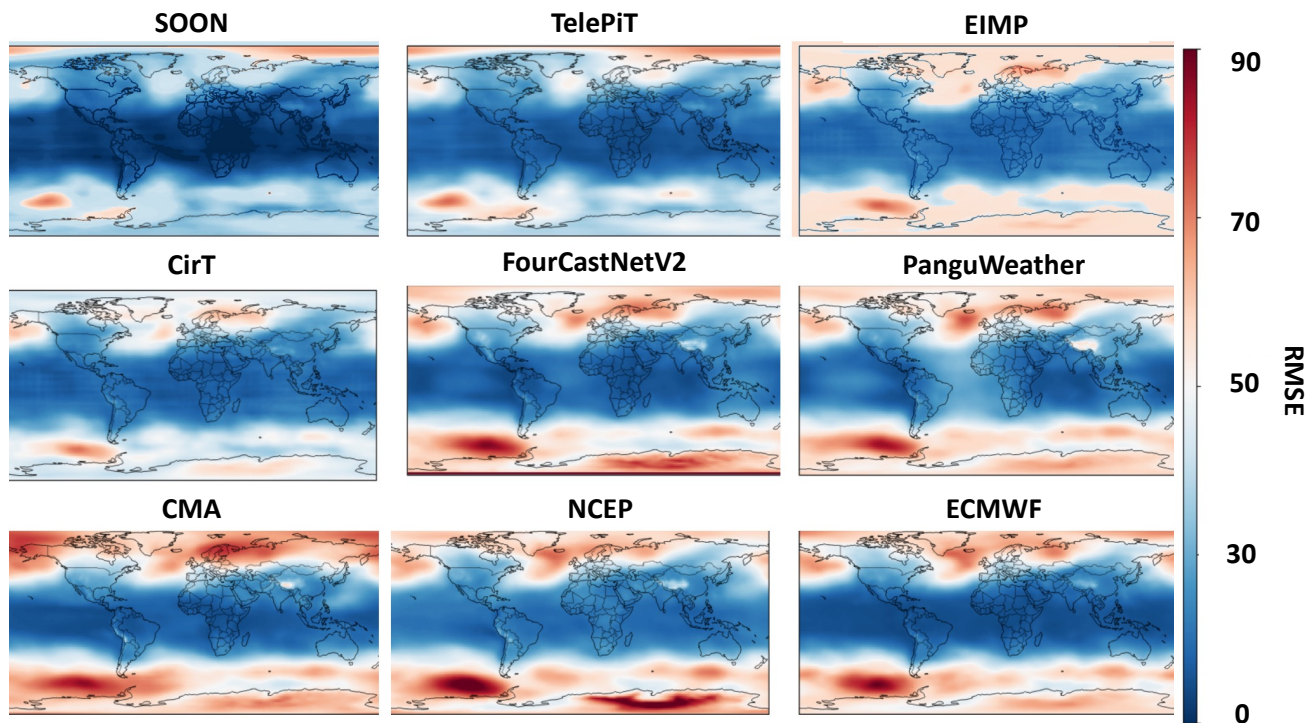


Figure 14. Global RMSE distribution for  $z850$  at weeks 3–4 lead time.

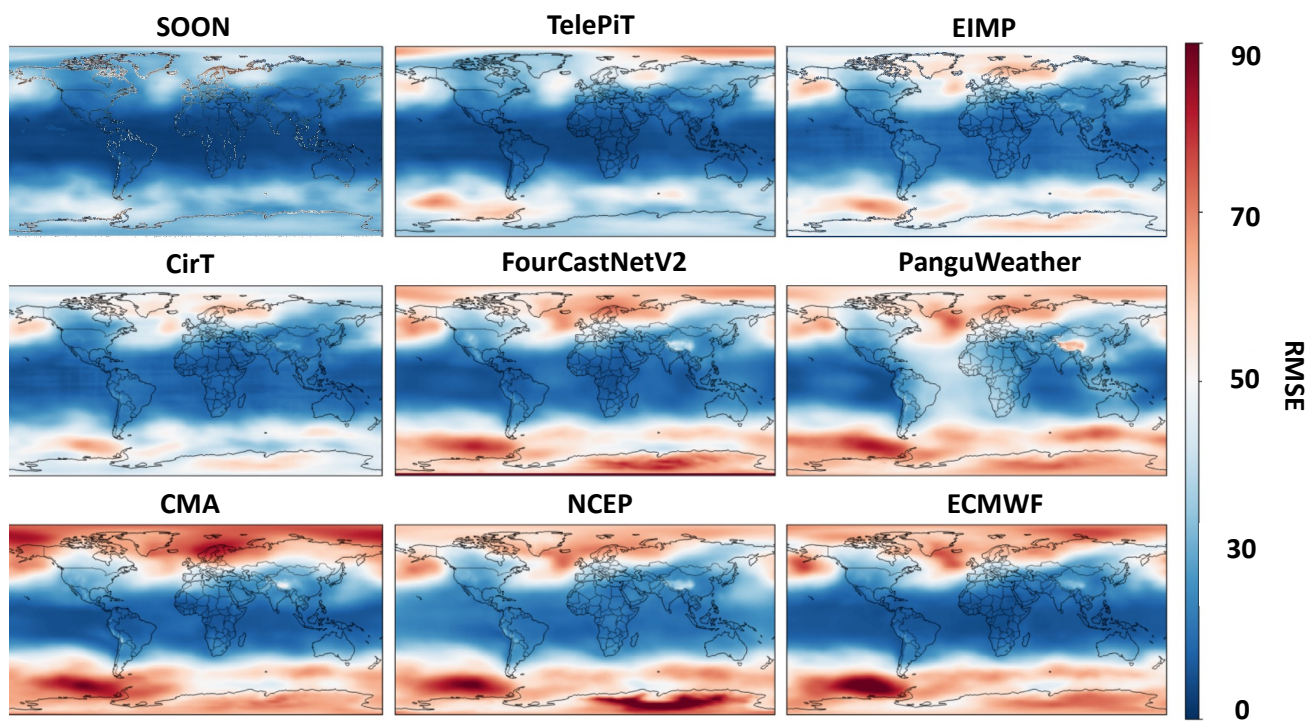


Figure 15. Global RMSE distribution for  $z850$  at weeks 5–6 lead time.

#### E.4. Vertical Profile Analysis

We further analyze the model’s performance across the vertical atmospheric column to ensure physical consistency at different altitudes. Figure 16 compares the RMSE of wind components ( $u, v$ ) against data-driven baselines, while Figure 17 benchmarks geopotential ( $z$ ) and temperature ( $t$ ) against operational NWP systems.

As shown in the heatmaps, SOON achieves the lowest normalized RMSE (indicated by the lightest colors) across almost all 13 pressure levels, from the surface (1000 hPa) up to the stratosphere (50 hPa). This vertical consistency is particularly notable in comparison to models like ClimaX and EIMP, which exhibit degradation in the upper atmosphere. The results demonstrate that SOON’s anisotropic embedding and operator design effectively capture the distinct dynamics of different atmospheric layers without requiring level-specific fine-tuning.

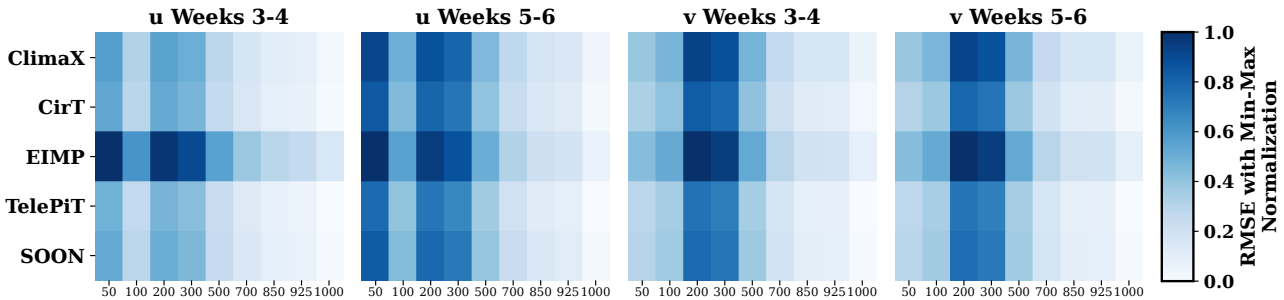


Figure 16. RMSE comparison between SOON and data-driven models on wind variables  $u$  and  $v$  across different pressure levels.

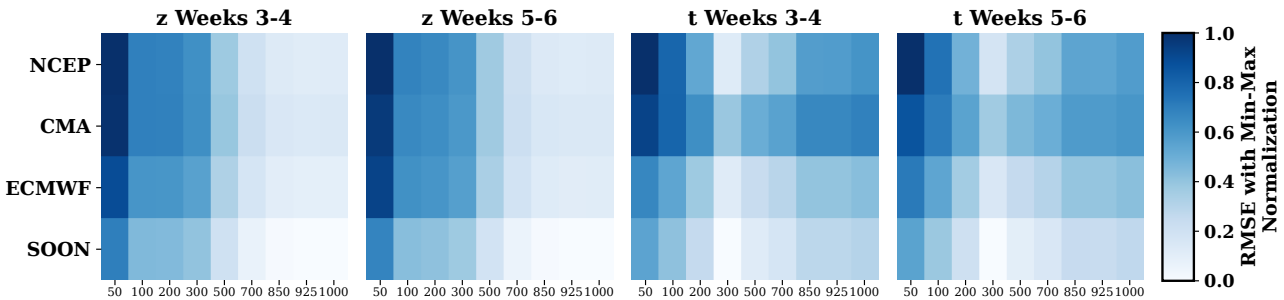


Figure 17. RMSE comparison between SOON and operational NWP systems on variables  $z$  and  $t$  across different pressure levels.

#### E.5. Daily Visualization and Temporal Stability

To probe fine-grained temporal stability, we trained SOON and other baselines to output the full daily trajectory. Figure 18 and Figure 19 visualize the day-by-day evolution of RMSE and ACC for weeks 3–4 (days 15–28) and weeks 5–6 (days 29–42), respectively. In the weeks 3–4 window (Figure 18), SOON consistently maintains superior performance across all variables. While baselines suffer from rapid degradation over time (manifested as steep error slopes), SOON exhibits a remarkably flat error growth rate. This advantage becomes even more pronounced in the extended weeks 5–6 window (Figure 19). For highly chaotic surface variables like  $v10$ , the performance gap between SOON and the nearest competitor widens significantly as the lead time increases. This empirical evidence confirms that our symmetric operator splitting scheme effectively mitigates the error accumulation inherent in long-horizon forecasting, maintaining high correlation (ACC) even deep into the subseasonal range.

#### E.6. Seasonal Robustness Analysis

S2S forecasting skill often varies significantly by season due to changing atmospheric dynamics. To evaluate robustness, we break down the testing set performance by month. Figure 20 to Figure 23 illustrate the monthly RMSE for key variables ( $z500, z850, t500, t850$ ). SOON demonstrates consistent superiority across all months of the year, outperforming both data-driven and numerical baselines. Whether in Northern Hemisphere winter (where baroclinic instability is high) or summer, SOON maintains the lowest error margins. This suggests that the model has successfully learned generalized representations of seasonal cycle dynamics rather than overfitting to specific regimes.

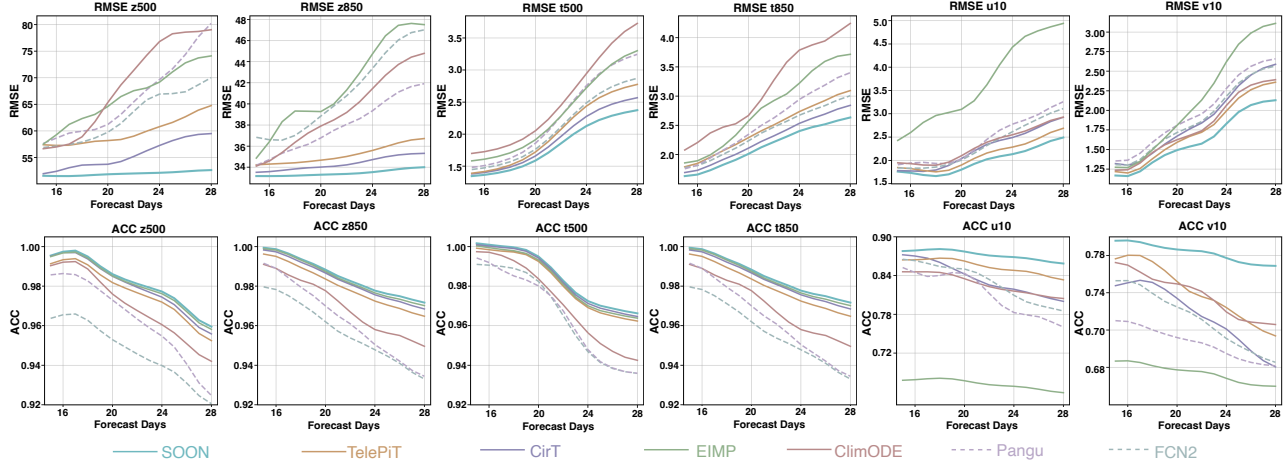


Figure 18. Daily RMSE and ACC variations across critical pressure level and single level variables during weeks 3–4 (Days 15–28).

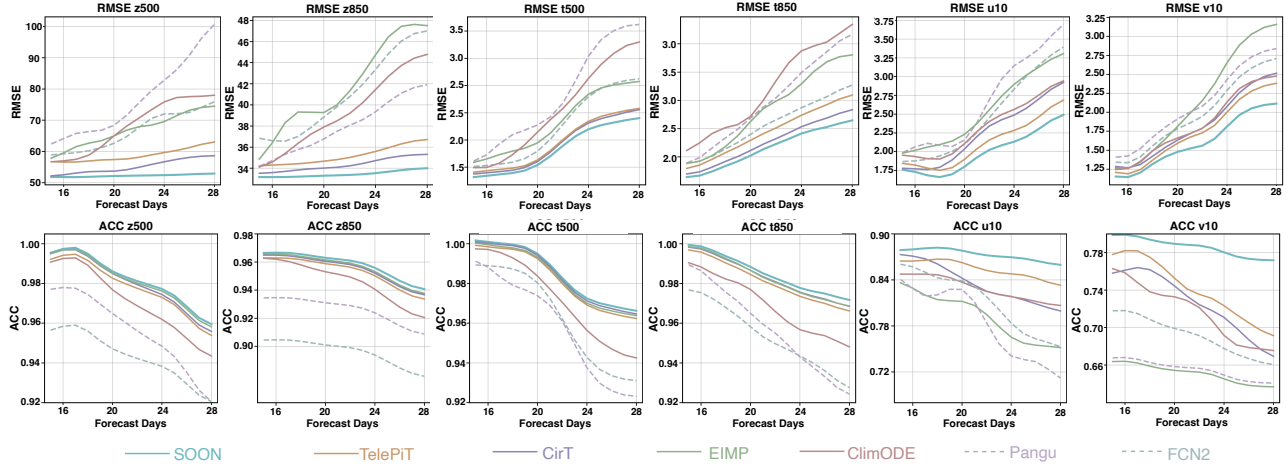


Figure 19. Daily RMSE and ACC variations across critical pressure level and single level variables during weeks 5–6 (Days 29–42).

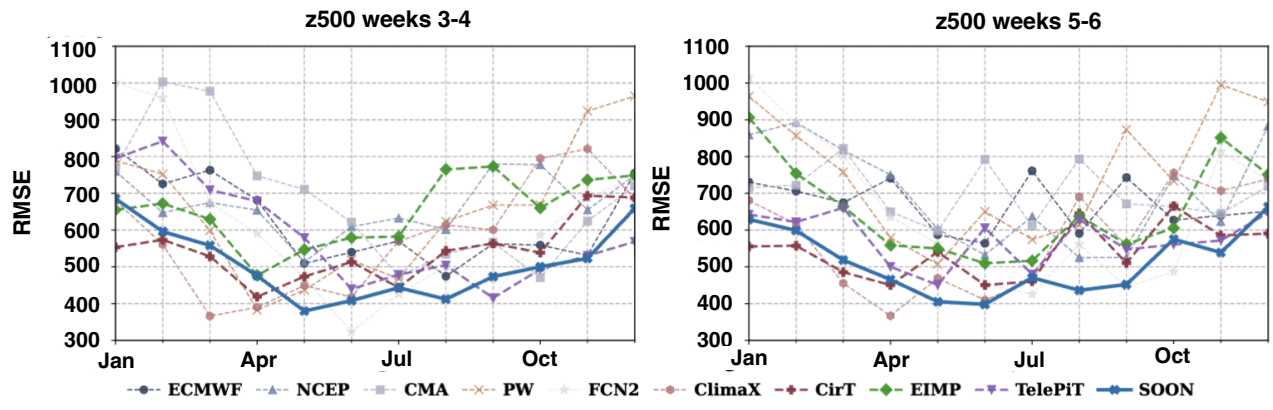


Figure 20. Monthly RMSE breakdown for  $z500$ : SOON consistently outperforms other models across all seasons.

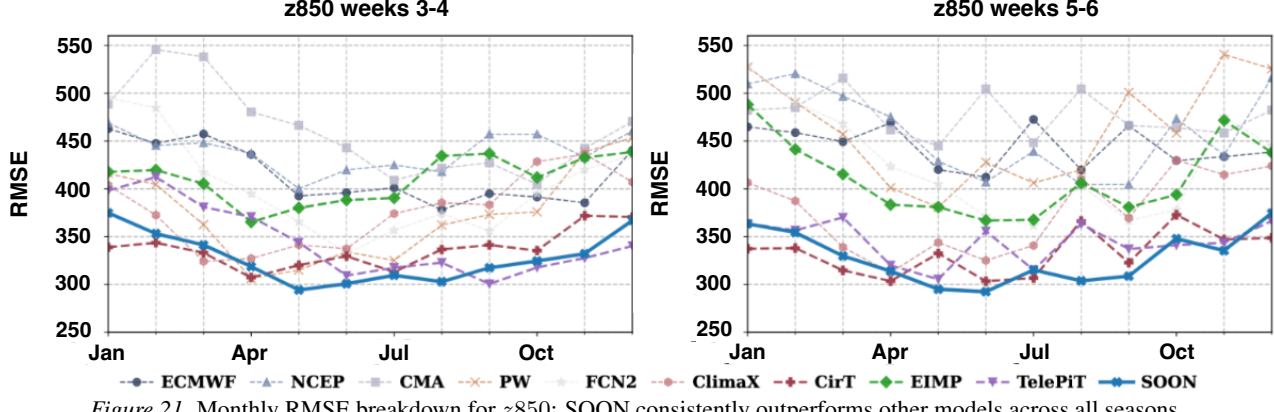


Figure 21. Monthly RMSE breakdown for  $z850$ : SOON consistently outperforms other models across all seasons.

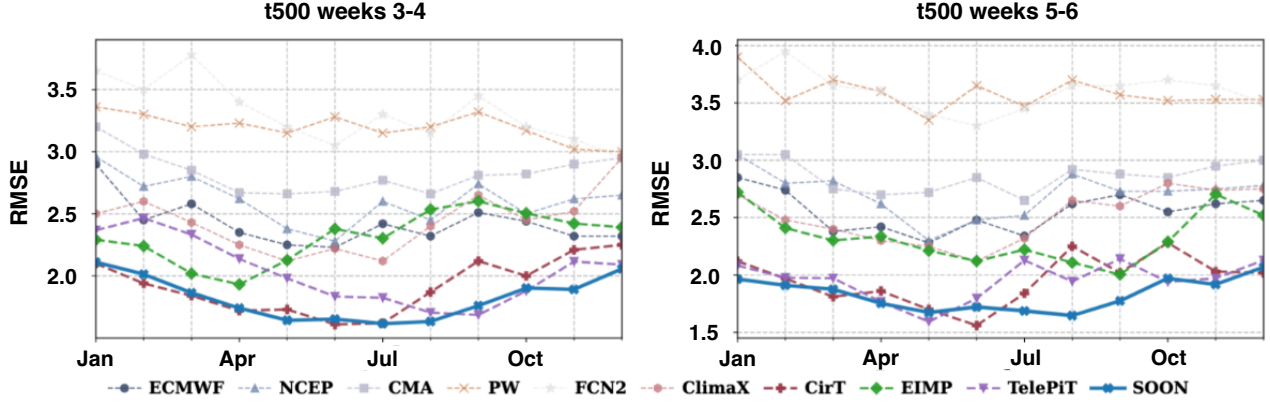


Figure 22. Monthly RMSE breakdown for  $t500$ : SOON consistently outperforms other models across all seasons.

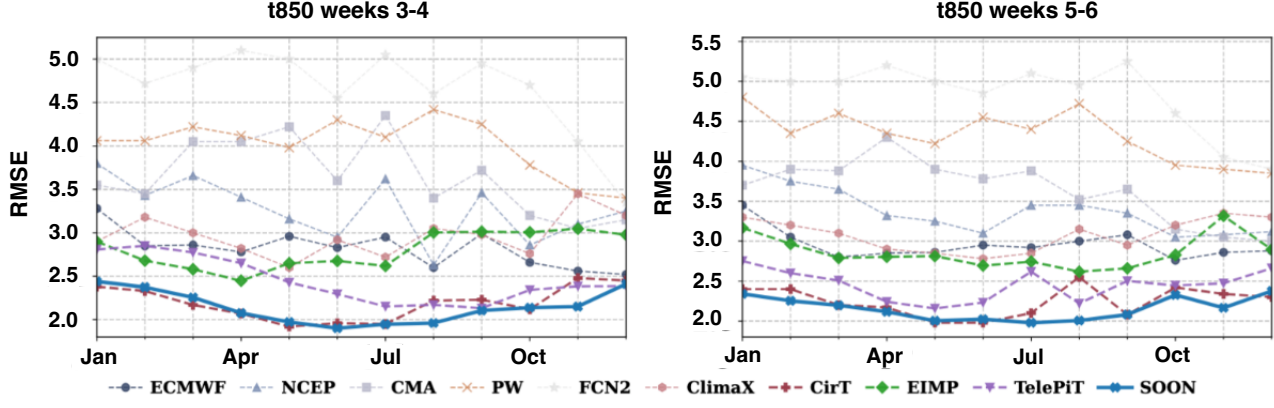


Figure 23. Monthly RMSE breakdown for  $t850$ : SOON consistently outperforms other models across all seasons.

## F. Limitations

While SOON achieves state-of-the-art performance, it currently relies on a deterministic regression objective, which does not explicitly quantify the forecast uncertainty inherent in chaotic S2S timescales. Additionally, due to computational constraints, our experiments are conducted at a  $1.5^\circ$  resolution, potentially under-resolving fine-grained sub-grid processes. Future extensions could incorporate probabilistic frameworks and higher-resolution training to further enhance utility for operational decision-making.